



Jiantong Li and Mikael Östling

Contents

21.1	Background of Graphene-Based Photodetectors	778
21.2	Performance Metrics of Photodetectors	778
21.2.1	Responsivity (R_{ph})	778
21.2.2	Quantum Efficiency	779
21.2.3	Noise Equivalent Power (NEP)	779
21.2.4	Detectivity (D^*)	779
21.2.5	Linear Dynamic Range (LDR)	779
21.2.6	Response Speed	779
21.2.7	Photoconductive Gain (G_{ph})	779
21.3	Physical Mechanisms for Photodetection	780
21.3.1	Photovoltaic Effect	780
21.3.2	Photothermoelectric Effect	780
21.3.3	Bolometric Effect	781
21.3.4	Plasma-Wave-Assisted Mechanism	781
21.3.5	Photogating Effect	781
21.4	Practical Realization of Graphene Photodetectors	781
21.4.1	Metal-Graphene-Metal (MGM) Photodetectors (PV and PTE Effects)	781
21.4.2	Graphene-Based Bolometers	782
21.4.3	Plasmonics-Enhanced Graphene Photodetectors	783
21.4.4	Detectors Based on Photogating	783
21.5	Graphene-Based Heterostructures for Photodetectors	785
21.5.1	Graphene/Silicon	785
21.5.2	Graphene/III–V Semiconductors	786
21.5.3	Graphene/Organic Semiconductors	787
21.5.4	Graphene/Perovskites	790
21.5.5	Graphene/Other 2D Materials	790
21.6	Integrated Graphene Photodetectors	795
21.6.1	Integration with Optical Cavity	795
21.6.2	Integration with Waveguides	795

21.7	Graphene Photodetectors with Special Geometry or Architectures	797
21.8	Conclusions and Outlook	797
References	801

Abstract

Photodetectors that convert light into electrical signals have become an indispensable element for a large number of technologies to enable extensive applications, ranging from optical communications to advanced imaging and motion detection, to automotive industry particularly including self-driving cars, and to astronomy and space exploration under harsh environment. The present photodetector market is predominated by silicon (CMOS-based) photodetectors. With the continuous growth of application areas, highly desired are photodetectors of higher performance in terms of speed, efficiency, detectable wavelength range, and integrability with semiconductor technology. These necessitate the development of new photodetectors based on special materials, rather than the conventional silicon single crystals, as building blocks for various advanced photodetection platforms. To this end, we summarize in this chapter the recent status of advanced photodetectors based on the emerging material, graphene. Our discussion includes the performance metrics, working mechanisms, practical implementation, as well as opportunities and challenges, for graphene-based photodetectors.

Keywords

Graphene · Photodetectors · Photodetection mechanism · Heterostructure · Optical cavity · Waveguide · Charge neutrality point · 3D substrates

J. Li · M. Östling (✉)
KTH Royal Institute of Technology, School of Electrical Engineering and Computer Science, Kista, Sweden
e-mail: jiantong@kth.se; mostling@kth.se

21.1 Background of Graphene-Based Photodetectors

Photodetection is becoming more and more important in a wide range of applications, including the ubiquitous visible light cameras and video imaging, medical X-ray and near-infrared (NIR) imaging, night-vision and shortwave infrared (SWIR) surveillance, motion detection, machine vision, gas sensing, optical communications, and so on [1–3]. It primarily makes use of semiconductors to transduce photons of different energies (determined by the bandgap of the semiconductors) into electrical signals for subsequent signal processing and applications. Up to date, the predominant materials for photodetectors in modern electronics and optoelectronics are still crystalline silicon, thanks to the high performance, low cost, manufacturing maturity, and high-level integration with CMOS electronics [4]. Over the past decade, amazing progress has been made in implementing a wide variety of optical and electro-optical devices in silicon, including laser sources, modulators, detectors, waveguides, and filters [5]. With the integration of CMOS technology, large-scale arrays of photodiodes and phototransistors have been developed for fabricating multifunctional image sensors. The applicability is, however, strongly limited by the property of silicon. For example, for applications in the infrared (IR) spectrum which is below the energy bandgap of silicon, photodetectors based on non-silicon materials become necessary. With the rapid development of emerging applications, such as self-driving cars, authentication systems, augmented and virtual reality, and point-of-need health care [3], a new and important demand has arrived for advanced photodetectors based on special materials that possess ultrafast conversion, high-frequency communications, significantly wider detectable spectrum, and readily tunable bandgaps.

During the past decade, graphene and other 2D materials have received great interest in a large variety of research fields. These materials possess a combination of many exceptional properties, such as adjustable energy bandgap, direct bandgap of many monolayer 2D materials, easy stacking of different 2D materials for vertical heterojunctions by van der Waals force, scalable synthesis process and compatibility with traditional microfabrication technique, as well as being ultrathin and flexible. All these properties make them potentially extremely interesting in photodetector applications [4, 6]. Among them, graphene is the most famous and appealing material for the development of photodetectors. First, its zero bandgap enables charge carrier generation by light absorption over a very wide energy spectrum, ranging from ultraviolet (UV) to visible to IR to terahertz (THz) spectral regimes with a constant absorbance of $\sim 2.3\%$ per layer [7]. Second, its high carrier mobility allows to convert rapidly photons

or plasmons to electrical currents or voltages [8, 9]. Third, the chemically passivated graphene surface greatly diminishes the influence of substrates and offers opportunities for integrated photonic devices on arbitrary substrates. Last, the strong quantum confinement resulting from the ultrathin 2D structure leads to many intriguing physical properties distinct from that of bulk materials [10]. For example, as a 2D material, its conductance is very sensitive to electrostatic perturbation by photogenerated carriers close to the surface [1], which is a desired property for high-gain photodetection.

Therefore, graphene can provide advanced or complementary techniques to silicon-based photodetectors. This chapter overviews the recent research progress of graphene-based photodetectors. We first summarize the performance metrics and basic physical mechanisms of photodetectors, then introduce the latest experimental realization of various photodetectors based on graphene, and finally discuss about the current challenges and outlook the future research directions.

21.2 Performance Metrics of Photodetectors

Typical figures of merit (FOMs) used to evaluate the performance of a photodetector include responsivity, detectivity, quantum efficiency, noise equivalent power (NEP), and response speed [1, 10]. Below is the introduction of these key metrics.

21.2.1 Responsivity (R_{ph})

Responsivity indicates the electrical output of a photodetector responding to an optical signal and is one of the most important characteristics for a photodetector. It is defined as the ratio of the photocurrent I_{ph} to the incident light power P_{in} , as

$$R_{ph} = I_{ph}/P_{in}; \quad (21.1)$$

or as the ratio of photovoltage V_{pc} to P_{in} as

$$R_{ph} = V_{pc}/P_{in}. \quad (21.2)$$

R_{ph} is often given in units of A/W. For a typical single-layer graphene (SLG) photodetector, responsivity is at the level of a few mA/W [10]. Also, responsivity is proportional to external quantum efficiency (EQE, the conversion rate from photons to electrons/holes) as

$$R_{ph} = EQE \times \lambda q/hc, \quad (21.3)$$

where λ is the incident light wavelength, q is the absolute value of electron charges, h is the Planck constant, and

c is the light speed, and hence, the responsivity depends on the wavelength. For broadband photodetection, constant responsivity across a large spectral range is preferred, while single-color detectors need a sharp peak in a narrow range. In practice, power independent responsivity is also desirable in systems that respond linearly to optical input [10].

21.2.2 Quantum Efficiency

The external quantum efficiency (EQE) is the ratio between the number of electron-hole (e-h) pairs per second collected to produce the photocurrent I_{ph} and the number of incident photons per second, as

$$\text{EQE} = (I_{\text{ph}}/q) / (P_{\text{in}}/E_{\text{ph}}), \quad (21.4)$$

where E_{ph} is the incident photo energy. Similarly, internal quantum efficiency (IQE) is the ratio between the e-h number and the number of absorbed photons, as

$$\text{IQE} = (I_{\text{ph}}/q) / (A_{\text{abs}}P_{\text{in}}/E_{\text{ph}}), \quad (21.5)$$

where A_{abs} is the absorbed fraction.

21.2.3 Noise Equivalent Power (NEP)

The noise equivalent power (NEP) is the minimum measurable power [11] or the signal power for a given bandwidth when the signal-to-noise ratio is unity [1]. It is calculated as

$$\text{NEP} = P_{\text{in}}/\sqrt{B} = i_{\text{n}}/R_{\text{ph}}, \quad (21.6)$$

where B is frequency bandwidth of the photodetector and i_{n} is the noise current. NEP is thereby in units of $\text{W Hz}^{-1/2}$.

21.2.4 Detectivity (D^*)

The specific detectivity is another typical FOM used to characterize photodetector performance. It is the minimum detectable level of light and is calculated as

$$D^* = \sqrt{A \cdot B}/\text{NEP} = \sqrt{A \cdot B} R_{\text{ph}}/i_{\text{n}}, \quad (21.7)$$

where A is the area of the photosensitive region. D^* is in units of Jones with $1 \text{ Jones} = 1 \text{ cm Hz}^{1/2} \text{ W}^{-1}$, in recognition of the work of R. C. Jones on sensitivity of radiation sensors [1].

21.2.5 Linear Dynamic Range (LDR)

The linear dynamic range (LDR) is the illumination intensity range within which the current response of a photodetector scales linearly with the light intensity [12] and is given by

$$\text{LDR} = 20 \log (J_{\text{ph}}/J_{\text{d}}), \quad (21.8)$$

where J_{ph} is the photocurrent density measured at a light intensity of 1 mW/cm^2 and J_{d} is the dark current density. In practice, a large LDR is desired so that a photodetector can detect both high- and low-intensity lights.

21.2.6 Response Speed

Response speed characterizes the capability of a photodetector to detect a signal at a certain rate [10]. In the frequency domain, speed is defined by the frequency at which responsivity is reduced to 50% of its maximum value. In the time domain, response time is used to characterize the response speed and defined as the time required for a transient output signal to reach 0.707 of its steady-state change upon a sudden change of the incident light. For some systems, the response time may be asymmetric between light switch ON and OFF. Then the response speed is characterized by the rise and fall times at 10% and 90% of the maximum photocurrent, respectively [12]. Fast operation (up to tens of GHz) is extremely important for telecommunication and interconnection, but for other applications such as sensing and imaging, only moderate speed (a few kHz) is required [10].

21.2.7 Photoconductive Gain (G_{ph})

Photodetectors are commonly benchmarked by their photoconductive gain, the number of carriers detected for each single incident photon. It can be quantified by the ratio of the lifetime (τ_{trap}) of the trapped carriers to the drift transit time (τ_{transit}), as

$$G_{\text{ph}} = \frac{\tau_{\text{trap}}}{\tau_{\text{transit}}}, \text{ with } \tau_{\text{transit}} = L^2/\mu V_{\text{bias}} \quad (21.9)$$

where L is the source-drain separation distance (channel length), μ is the carrier mobility, and V_{bias} is the bias voltage.

It is worth mentioning that in many cases, trade-offs have to be made between different FOMs [10]. For instance, responsivity can be effectively increased through integration with extra light absorbers, but often the response speed is sacrificed. More relevant discussion is included in the following sections.

21.3 Physical Mechanisms for Photodetection

Several different mechanisms have been realized in graphene and 2D materials-based photodetection and other optoelectronic applications, including the photovoltaic effect, the photo-thermoelectric effect, the bolometric effect, the photogating effect, and the plasma-wave-assisted mechanism, as summarized in Fig. 21.1 and detailed below.

21.3.1 Photovoltaic Effect

Photovoltaic (PV) current is generated through separating photon-induced electron-hole (e-h) pairs either by built-in electric fields at a p-n junction or a metal-semiconductor Schottky junction [13, 14] (Fig. 21.1a) or by the external electric field under an applied bias voltage. As graphene is a semimetal, external electric field is not favored due to the very high dark current and power consumption. The built-in field can be created by several techniques, including local chemical doping [15], splitting gates [13, 16], or inherent work function difference between graphene and a contacting metal [17]. In a splitting gate structure, the doping can be tuned to be either p- or n-type, depending on the applied gate voltages. In graphene-metal junctions, the doping is fixed, typically as p-type for metals that have higher work function than graphene (4.45 eV). The electric field is the only factor to determine the photocurrent. Thus, photocurrents switch sign when going from p-n junction to n-p junction or from p-p⁺ junction to p⁺-p junction [1].

A special phenomenon for graphene is the carrier multiplication (Auger-type) impact ionization [10] where the strong carrier-carrier scattering, owing to the zero bandgap,

leads to the conversion of one high-energy electron-hole pair into multiple electron-hole pairs of lower energy [18–20], which potentially enhances the overall photodetection efficiency. This process fundamentally differs from the impact ionization in traditional semiconductors where a sufficiently large electric field increases the kinetic energy of a carrier which then loses energy to create other low-energy carriers, resulting in avalanche breakdown [10].

21.3.2 Photothermoelectric Effect

The photothermoelectric (PTE) effect refers to the conversion of light-induced temperature gradient to an electric voltage. Due to the large thermal conductivity of graphene, the PTE effect generated by lattice heating is not significant. In contrast, significant photovoltage can be produced by photogenerated hot electrons. Due to the strong electron-electron interactions, photo-excited electron-hole pairs lead to ultrafast (~ 10 – 50 fs) heating of the carriers in graphene [21–23]. Because of the large optical phonon energy in graphene (~ 200 meV), the carriers can remain at a temperature much higher than the lattice temperature for a few picoseconds. The final thermal equilibration between the hot electrons and the lattice needs a nanosecond timescale due to the slower scattering between charge carriers and acoustic phonons [24, 25]. As a result, the temperature difference between hot carriers (e.g., in two graphene regions with different doping, Fig. 21.1b) can produce a photovoltage, $V_{\text{PTE}} = (S_1 - S_2)\Delta T_e$, where $S_{1,2}$ (in V K^{-1}) is the thermoelectric power (Seebeck coefficient) in the two different graphene regions and ΔT_e is the electron temperature difference between the regions. Photoresponse generated by hot carriers rather than lattice heat-

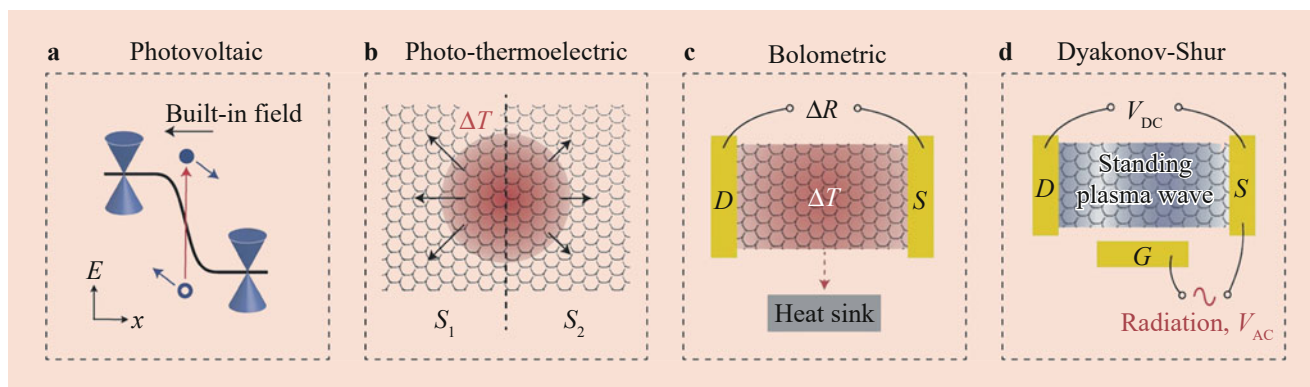


Fig. 21.1 Schematic of four typical photocurrent generation mechanisms: (a) photovoltaic (PV) effect where electron (solid circle)-hole (open circle) separation by an internal (built-in) electric field, (b) photothermoelectric (PTE) effect, (c) bolometric effect, and (d) plasma-wave-assisted mechanism. In (b, c), red-shaded area indicates elevated electron temperature where ΔT is the temperature gradient, ΔR is the

resistance across the channel, and S_1 and S_2 are Seebeck coefficient in graphene areas with different doping. In (c, d), S and D indicate source and drain, respectively, and G the gate; V_{DC} photogenerated dc voltage; V_{AC} , ac voltage applied to the gate. (Adapted with permission from [1] Copyright (2014) Springer Nature)

ing can achieve wide bandwidths, like in the case of PV photodetectors. The PTE effect typically dominates in graphene p-n junctions [16, 26] or in suspended graphene [27].

21.3.3 Bolometric Effect

The bolometric effect refers to the change in the transport conductance caused by light heating (Fig. 21.1c). Because this photodetection relies on light-induced conductance change, instead of direct photocurrent generation, it requires an externally applied bias and can operate on homogeneous graphene (no p-n junction is needed). The conductance change may result from the temperature-dependent carrier mobility and/or the change of carrier density.

21.3.4 Plasma-Wave-Assisted Mechanism

In a field-effect transistor (FET), when exposed to an oscillating radiation field (Fig. 21.1d), a finite dc voltage may be generated. Based on this rectification, Dyakonov and Shur [28, 29] proposed a photodetection scheme. The 2D electron gas hosted in an FET can act as a cavity for plasma waves (collective density oscillations) [1]. For weakly damped plasma waves (the transport time of a plasma wave from the source to the drain is shorter than the momentum relaxation time), their constructive interference can be used to detect the radiation with a resonantly enhanced response. This is the so-called resonant regime of plasma-wave photodetection and can produce a signal 5–20 times stronger than the broadband nonresonant signal in the case of overdamped plasma waves (plasma waves launched at the source decay before reaching the drain) [29]. Dyakonov and Shur [29] showed that even if the incoming field is ac, the photovoltage response of a 2D electron system in a FET still contains a dc component, which provides rectification of the signal. This is particularly useful for the detection of THz radiation. Detection of THz radiation in graphene FETs has been theoretically discussed [30] and experimentally demonstrated [31, 32].

21.3.5 Photogating Effect

The photogating effect is based on light-induced modification of the graphene carrier density and hence its conductance [1]. Typically, one type of photogenerated carrier is captured by the trap centers or transferred from external source, both of which result in change of carrier density. Therefore, the photoconductive gain, G_{ph} , can be strongly enhanced by using a high-mobility conductor, such as graphene, and by a long lifetime. Also responsivity based on the photogating effect can be very large, up to millions of A/W because

photo-induced carriers can move several times through the channel before recombination, providing a significant optical gain [10]. In contrast, responsivity in the PTE and bolometric regimes is limited to less than a few mA/W. However, longer photocarrier lifetime reduces the operation speed. And the photoconductive detectors may exhibit high dark current, which influences the noise equivalent power and detectivity.

21.4 Practical Realization of Graphene Photodetectors

In practice, a large variety of graphene photodetectors have been developed based on different mechanisms, heterogeneous junctions with other materials, and advanced architectures. This section summarizes the representative implementations of these photodetectors.

21.4.1 Metal-Graphene-Metal (MGM) Photodetectors (PV and PTE Effects)

The MGM photodetectors (Fig. 21.2) were the first and simplest class of graphene-based photodetectors to be investigated. In early reports [9, 33–35], photocurrent was generated through the PV effects by local illumination of one of the metal/graphene interfaces of a back-gated graphene FET. The field arising from charge transfer from the contact metal to graphene [36, 37] can thus be adjusted by choosing the proper metal [34, 38]. Besides the PV effect, the PTE effect may also dominate the photoresponse in the vicinity of p-n junctions or interfaces of SLG and bilayer graphene (BLG) [26, 27, 39]. The PTE effect can be distinguished from the PV effect according to the sign of the photocurrent. Different from the PV current, the PTE current reverses the direction in bipolar p-n junctions and also unipolar p^+ -p or n - n^- junctions [26], due to the change of transconductance upon transport between different doping region transports. The relative contributions of the PTE and PV effects to the photocurrent can be controlled through adjusting the wavelength. At longer wavelengths, the PV effects become pronounced.

Because the photocurrent is only generated in the vicinity of metal/graphene interface region, interdigitated finger structures (Fig. 21.2b) with asymmetric electrode metals are often used to increase the effective photodetection area [9] and suppress the dark current. Thanks to the high carrier mobility and short carrier lifetime in graphene, MGM photodetectors can operate at high data rates. In single metal-graphene junctions, it has been demonstrated that photoresponse does not degrade at a modulation frequency of 40 GHz [8] and all-optical measurement gave an intrinsic bandwidth of 262 GHz. It is worthy of mentioning that

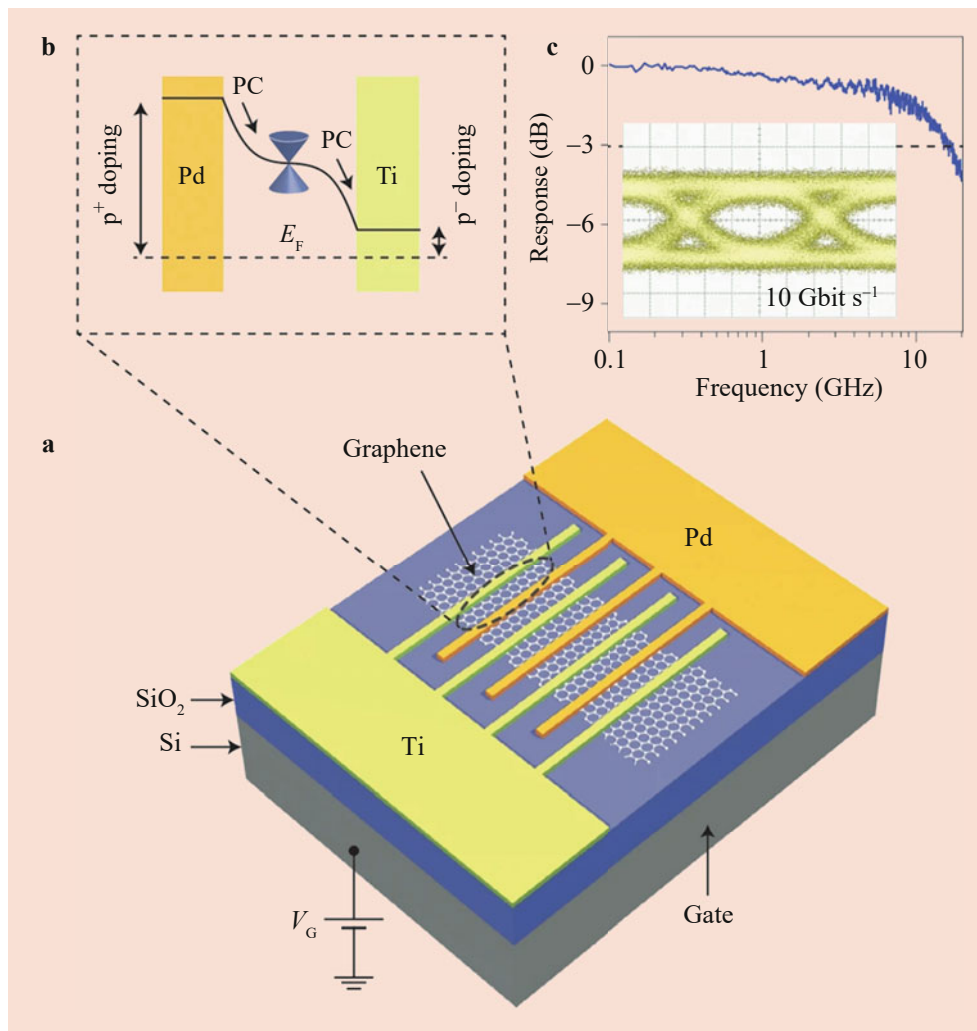


Fig. 21.2 A typical metal-graphene-metal photodetector with asymmetric contacts: (a) Three-dimensional schematic. (b) Energy band and profile, where the arrows and Dirac cone indicate the electron flow and the charge neutrality point, respectively. PC stands for photocurrent.

(c) High-frequency response. Inset: eye diagram. (Reproduced with permission from [9] Copyright (2012) Springer Nature for (a, c) and from [1] Copyright (2014) Springer Nature for (b))

both PV and PTE effects are compatible with the high bandwidths owing to the decoupling of electron and lattice temperature [1].

21.4.2 Graphene-Based Bolometers

Bolometric responses have been observed at room temperature when SLG is biased [17, 40]. The dominant factor for the conductance change (either photo-induced excess carriers or temperature-dependent mobility) can be controlled through adjusting Fermi level (E_F) of graphene [17]. However, the weak temperature dependence of the electrical resistance in graphene [41] makes it difficult to extract the temperature difference through electrical transport measurements, resulting in a small responsivity at the level of 0.2 mA/W [17]. To solve this problem, several strategies have been demon-

strated, such as introducing disorder [42], patterning nanostructures [43], and opening a bandgap in bilayer graphene [40]. As shown in Fig. 21.3a, an extra optically transparent top gate was applied to a dual-gated bilayer graphene device (Fig. 21.3a) to open a bandgap at the Dirac point [44, 45] and obtain electron temperature (T_e)-dependent resistance [44] to generate bolometric photoresponse [40]. The devices attain a high voltage of $2 \times 10^5 \text{ V W}^{-1}$ and a very low NEP of $33 \text{ fW Hz}^{-1/2}$ at 5 K as compared with commercial silicon bolometers ($200\text{--}2000 \text{ fW Hz}^{-1/2}$). Their intrinsic speed exceeds 1 GHz at 10 K, three to four orders of magnitudes higher than commercial silicon bolometers and superconducting transition-edge sensors at similar temperatures. In addition, a graphene-superconductor tunnel junction bolometer (Fig. 21.3b) has also been demonstrated at radio-frequency regions [46], which should also apply for optical detection [1].

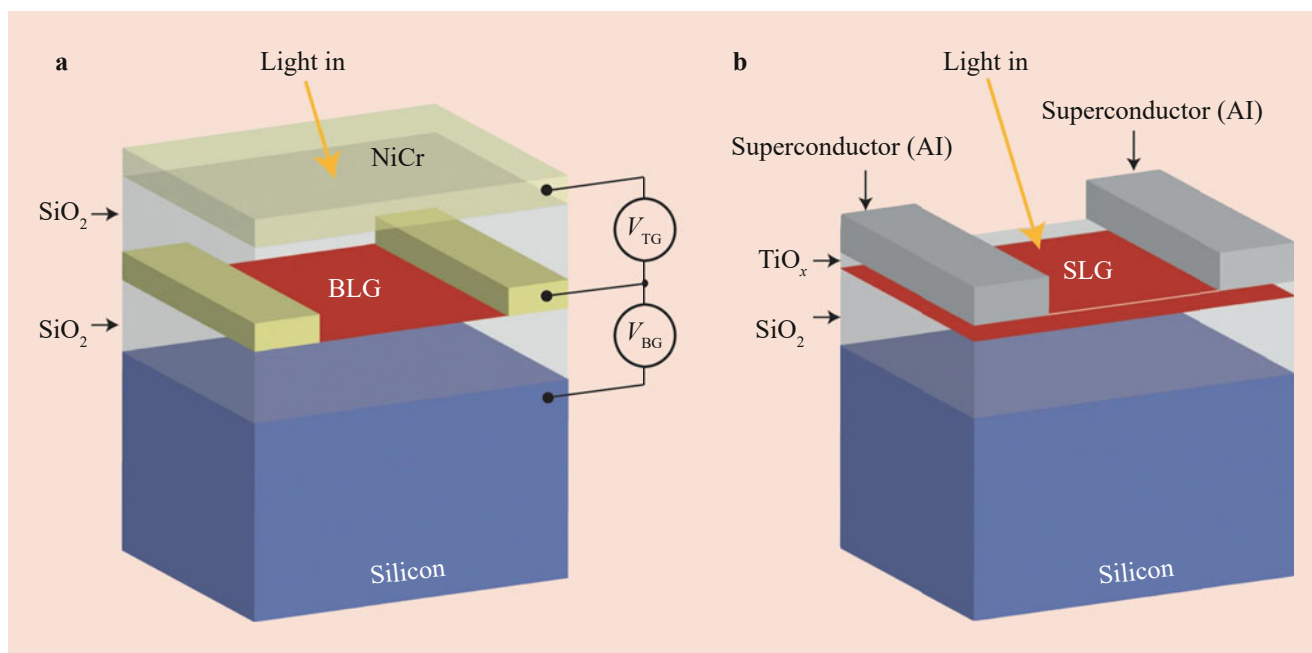


Fig. 21.3 Graphene-based bolometers. (a) Device structure of a dual-gated bilayer graphene bolometer [40]. V_{TG} and V_{BG} are top gate bias and back-gate bias, respectively. (b) Device structure of an SLG-

aluminum tunnel junction bolometer [46]. (Reproduced with permission from [1] Copyright (2014) Springer Nature)

21.4.3 Plasmonics-Enhanced Graphene Photodetectors

The excitation of surface plasmons is an effective method to increase the photoresponse of graphene photodetectors. Localized plasmons in metal nanostructures were first used along with graphene to obtain surface-enhanced carrier density (Fig. 21.4a, b) [48] and Raman scattering [50] and to enhance strong fields in subnanometer gaps [51]. The introduction of plasmonic nanostructures near the contacts [49] of graphene-based photodetectors (Fig. 21.4c–e) has also been demonstrated to significantly improve the device performance (Fig. 21.4e). In addition, nanostructures with geometries resonant at desired wavelengths offer opportunities for selective amplification, potentially allowing light filtering and detection, as well as polarization determination in a single device [52]. As compared with traditional devices, the plasmonic structures greatly improve the frequency performance because their contribution to the capacitance (fractions of femtofarads) is negligible, whereas they can significantly reduce the contact resistance.

Besides, field enhancement by plasmons can also improve photodetection performance due to the intrinsic collective charge oscillations of the 2D electron liquid inside graphene (Fig. 21.4f, g). The high carrier mobility and 2D character of graphene greatly enhance its light absorption [53], which provides an ideal solution to make use of graphene as both photodetector and plasmonic enhancers. As is shown

in Fig. 21.4e, graphene nanoribbon arrays on SiO_2 with different widths have been demonstrated as room-temperature tunable IR photodetectors with a performance improvement by 1500% [47].

21.4.4 Detectors Based on Photogating

A gain mechanism that provides multiple electrical carriers per single incident photon is crucial for photon detection at very low intensities, even approaching the single-photon level [1]. This can be achieved by effectively absorbing light with appropriate sensitizing centers and then transferring the carriers into the conductor (photogating effect, Fig. 21.5a) [54, 55]. It often results in a shift in the typical resistance versus gate-voltage curve, as shown in Fig. 21.5b. Graphene is excellent for room-temperature high-gain photodetection because of its high mobility (thus short carrier transit time) and its strong conductance dependence on the electrostatic perturbation by photogenerated carriers close to the surface. As a good example, colloidal quantum dots, such as PbS [54] (Fig. 21.5), CdS, or ZnO [56], are widely used to sensitize graphene. They have strong light absorption and bandgap tunability and can cover the absorption range from ultraviolet to SWIR [57]. Graphene decorated with PbS quantum dots can exhibit a high gain of 10^8 corresponding to $R_{ph} \sim 10^7$ A/W (at room temperature) for low light intensities

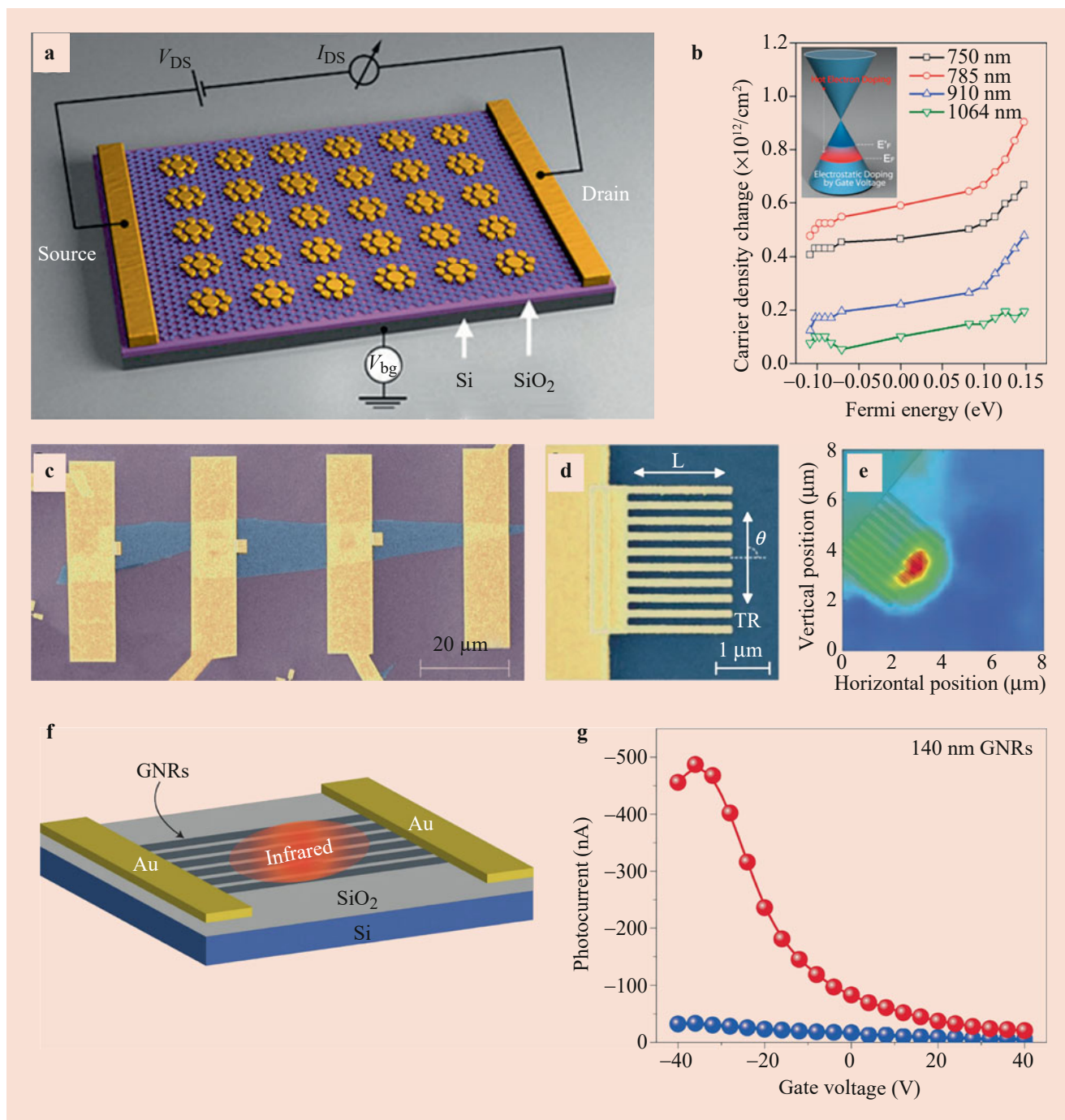


Fig. 21.4 Photodetectors enhanced by metallic plasmonic nanostructures and intrinsic plasmons. **(a)** Schematic of plasmonic antennas on SLG. **(b)** Light-induced carrier density change with respect to Fermi energy at selected wavelengths. Inset: energy diagram of the graphene Dirac cone, with antenna, under laser excitation. **(c)** Photodetectors with plasmonic nanostructures at the contacts (in false colors). Blue, graphene; purple, SiO₂ (300 nm); yellow, Ti/Au electrodes. **(d)** A contact with a “finger structure” in **(c)**. Longitudinal (L) and transverse (TR) incident light polarizations are indicated. **(e)** Photovoltage map of one of

the nanostructured contacts, similar to the one shown in **(d)**. Color scale runs from $-4 \mu\text{V}$ (blue) to $12 \mu\text{V}$ (red). **(f)** Schematic of a nanoribbon array infrared photodetector. GNRs: graphene nanoribbons [47]. **(g)** Photocurrent against gate voltage for the GNR (ribbon width 140 nm) detectors with (red spheres) and without (blue spheres) plasmon excitation [47]. (Reproduced with permission from [48]. Copyright (2012) American Chemistry Society for **(a, b)**, from [49] Copyright (2011) Springer Nature for **(c–e)**, and from [1] Copyright (2014) Springer Nature for **(f, g)**)

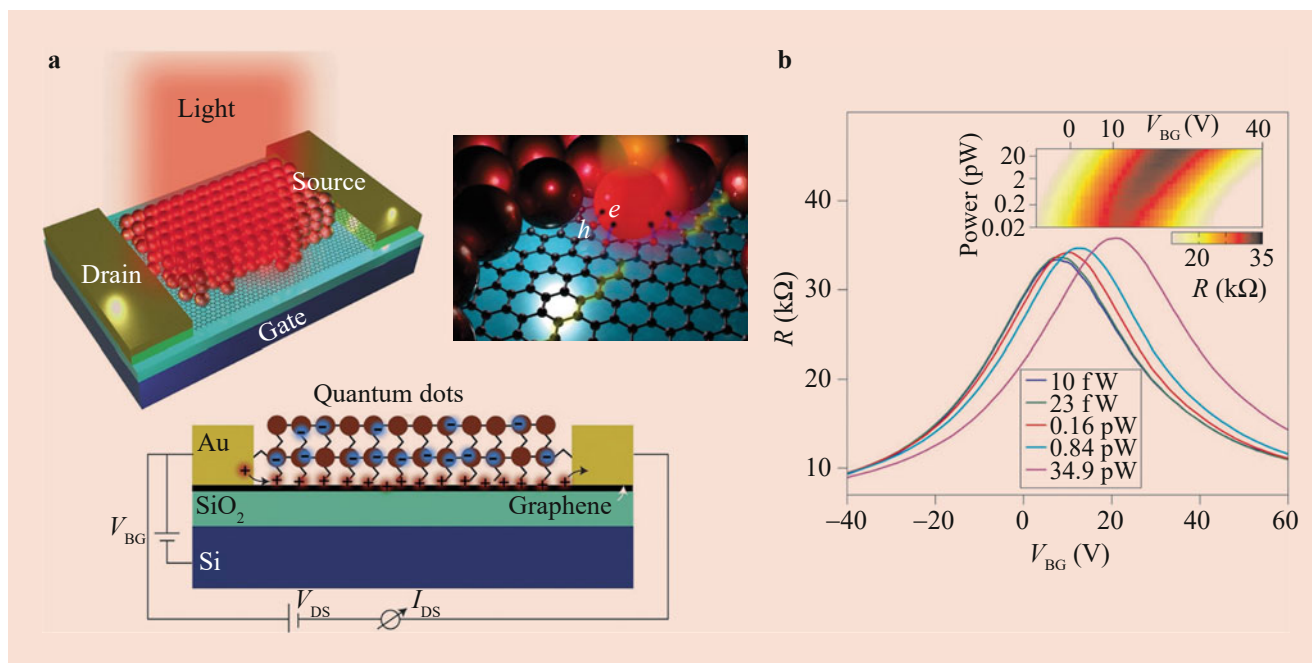


Fig. 21.5 Graphene photodetectors with sensitizing centers (photogating effects). (a) Schematics of photodetectors based on quantum dots (top left and bottom) and the e - h separation in the quantum dots (top right). (b) The dependence of resistance on the back-gate voltage

(V_{BG}) in a graphene-PbS quantum dot hybrid structure. Under stronger illumination, the Dirac point shifts to higher V_{BG} due to the photogating effects. Inset: map of graphene resistance against optical power. (Reproduced with permission from [54] Copyright (2012) Springer Nature)

$\sim 10^{-14}$ W [54]. Given the high QE ($>25\%$), specific detectivity of 7×10^{13} Jones, video imaging speed ~ 30 – 60 Hz, and low NEP $\sim 10^{-17}$ W (at the noise floor of $0.1 \Omega \text{ Hz}^{-1/2}$), this hybrid system is a promising platform for visible and SWIR applications [1].

21.5 Graphene-Based Heterostructures for Photodetectors

Although graphene-based optoelectronic devices are being extensively studied and some have already reached a competitiveness level comparable to conventional semiconductor devices [1, 58], several intrinsic drawbacks of graphene still limit the applicability, including low light absorbance (only 2.3%) of SLG and short light-matter interaction length causing ineffective light harvesting, ultrashort lifetime of excitons in pure graphene leading to fast carrier recombination, and low sensitivity of graphene-based detectors. To essentially address these drawbacks, various graphene-based heterostructures have been developed for photodetector applications to improve the performance [1, 12]. Here, we summarize these heterogeneous structures with different materials.

21.5.1 Graphene/Silicon

Graphene/silicon Schottky junctions are among the most studied devices for graphene heterojunction photodetectors where silicon absorbs light and graphene acts as an optically transparent charge carrier collector. The zero-gap and semimetallic properties of graphene are very promising for the wideband photodetection from microwave to UV regimes. The heterojunctions significantly increase the speed of carrier separation due to the built-in electric field, while the photocarrier lifetime is not reduced evidently under 1550 nm illumination [61]. As a result, an IQE of 10% was obtained for graphene/Si junctions in contrast to an IQE $\sim 1\%$ in regular Schottky junctions. The device performance can be further improved through introducing metal nanoparticles (such as Pt nanoparticles) [62] or an extra MoO₃ layer [63] for surface doping. To reduce the leakage current in the graphene/Si Schottky junctions, a thin interface layer of SiO₂ can be employed [64]. In particular, through the scanning photocurrent measurement technique, Riazimehr et al. [59] find that higher photocurrent (corresponding to a responsivity about 0.3 A/W) is generated in the graphene/SiO₂/Si region as compared to the graphene/Si region (responsivity about 50 mA/W) at reverse biases above a threshold voltage (Fig. 21.6a, b). This behavior is independent of excitation

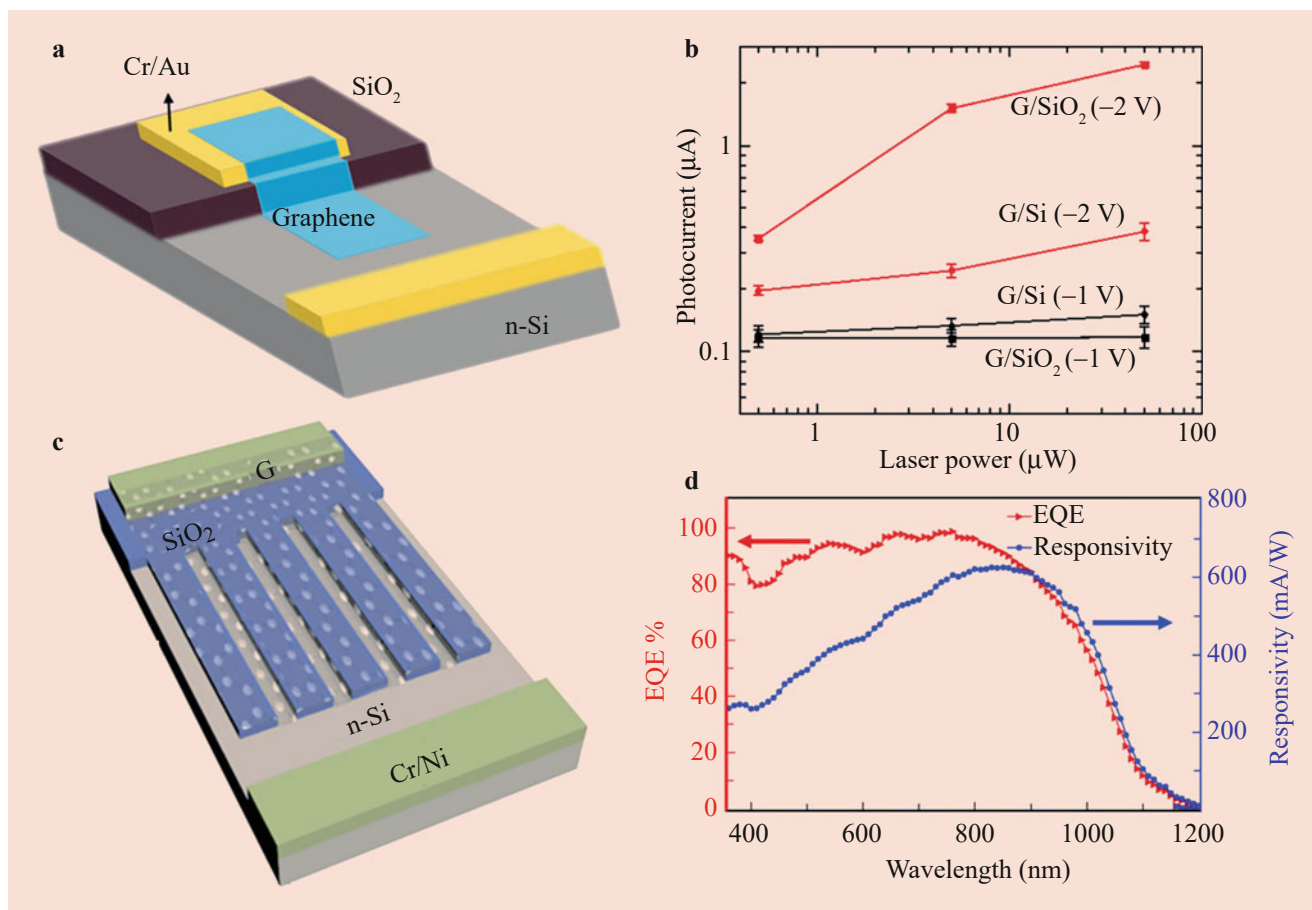


Fig. 21.6 Photodetectors based on graphene/silicon heterostructures. (a) Schematic of a graphene/silicon photodiode. (b) Photocurrent against laser power for the photodiode in (a) at different reverse biases in the graphene/Si (G/Si) and graphene/SiO₂ (G/SiO₂) regions. (c) Schematic of the patterned graphene/silicon photodiode where graphene is in contact with interdigitated SiO₂/Si structured substrates. (d) Wavelength-dependent EQE and responsivity of the patterned photo-

diode in (c). (Reproduced with permission from [59] Copyright (2017) American Chemistry Society (<https://pubs.acs.org/doi/full/10.1021/acsp Photonics.7b00285>), further permission should be directed to ACS) for a, b and from [60] Copyright (2018) American Chemistry Society (<https://pubs.acs.org/doi/10.1021/acsp Photonics.8b00951>), further permission should be directed to ACS) for c, d)

laser power and could be ascribed to the formation of an inversion layer in the Si layer under the graphene/SiO₂ junction. Furthermore, when the graphene/SiO₂/Si region is patterned in interdigitated structure (Fig. 21.6c) [60], a high EQE of >80% is achieved for wavelengths ranging from 380 to 930 nm with the maximum EQE of 98% at 850 nm, where the responsivity also peaks to 635 mA/W (Fig. 21.6d).

The performance improvement can also rely on porous Si and Si NWs. As shown in Fig. 21.7a–c, the graphene/porous Si Schottky diodes have achieved an excellent performance of responsivity up to about 0.3 A/W, as well as 60% EQE and 3 μs response time [65]. Alternatively, the NIR photodetectors based on a graphene/silicon nanowire array decorated with Au nanoparticles (Fig. 21.7d) [66] exhibit high performance of 10⁶ light-to-dark current ratio (Fig. 21.7e) and high response speed (rise/fall time of 73/96 μs, Fig. 21.7f),

possibly resulting from the enhanced optical absorption due to the strong optical trapping effect of silicon nanowire arrays and the surface plasmon coupling by Au nanoparticles.

21.5.2 Graphene/III–V Semiconductors

Heterojunctions between graphene and III–V semiconductors have also been used for photodetectors. GaN and GaAs are direct bandgap semiconductors with excellent optical/electrical properties for various photodetection applications. Graphene/GaN Schottky diode [69] has shown high light-to-dark current ratio (10⁵) under UV illumination. In addition, graphene/GaN nanowire array (Fig. 21.8a–c [67]) shows extremely high responsivity of 25 A/W at 357 nm, validating the promising application of graphene/GaN junctions in the UV region. On the other hand, graphene/GaAs Schottky

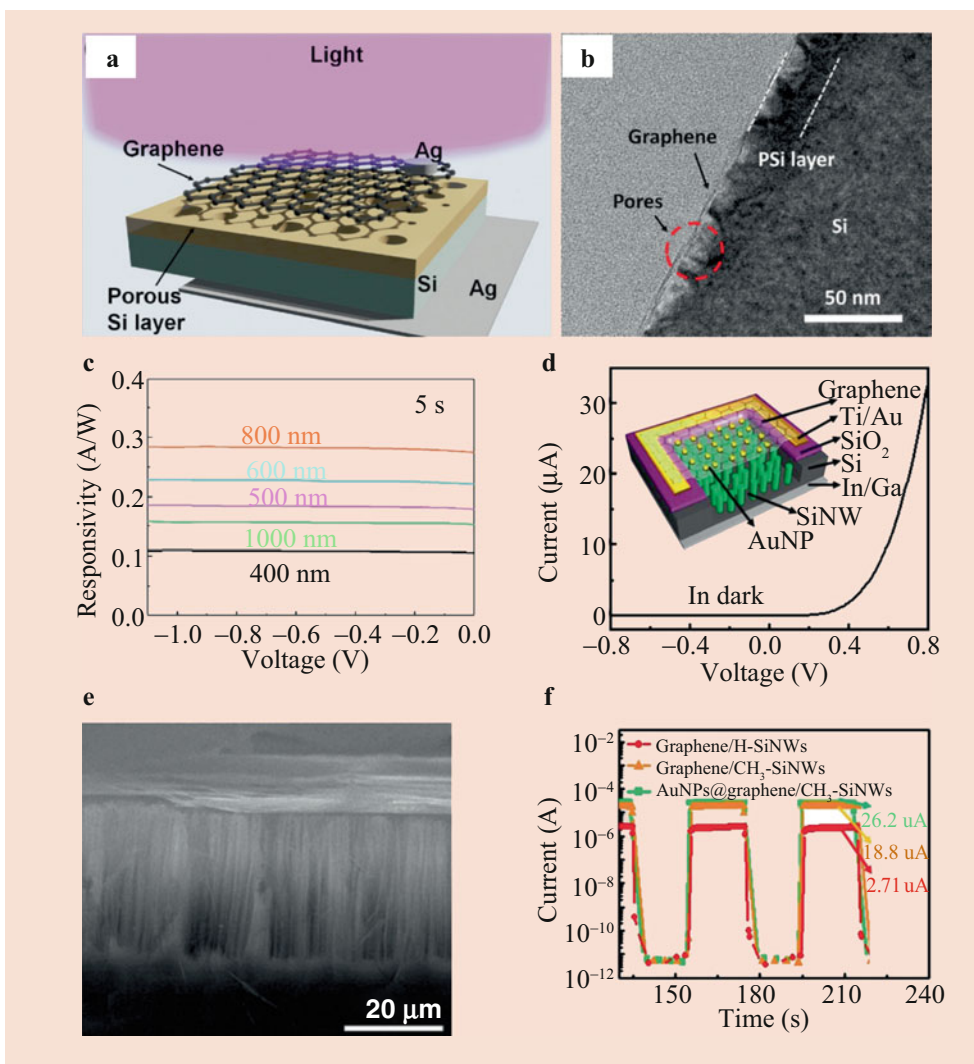


Fig. 21.7 Photodetectors based on graphene/silicon (porous or nanowire) heterostructures. (a) Schematic of graphene/porous silicon/n-silicon photodetectors with Ag top and bottom electrodes under light illumination [65]. (b) Cross-sectional transmission microscopy (TEM) image of graphene/porous Si junction. (c) Responsivity of a graphene/porous Si photodetector under illumination at various wavelengths from 400 to 1000 nm. (d) Schematic (inset) and current-voltage curves of the graphene/silicon nanowire array photodetectors

enhanced by Au nanoparticles [66]. (e) Cross-sectional SEM image of the graphene/Si nanowire photodetector. (f) Photoresponse of three representative devices under alternate switching on and off of the NIR illumination (wavelength 850 nm, at the power of 3 mW/cm²) at zero bias voltage. (Reproduced with permission from [65] Copyright (2014) American Chemical Society for a–c and from [66] Copyright (2014) Springer Nature for d–f)

junctions are promising for NIR light detection [68]. As shown in Fig. 21.8d–f, graphene/GaAs nanocone arrays exhibit reproducible photodetector performance of 10⁴ light-to-dark current ratio, 1.73 mA/W responsivity, and fast response speed with rise/fall times of 72/122 μs. Recently [70], using a thin layer of AlO_x as a surface protective layer to suppress carrier recombination and a barrier to reduce dark current, the performance of graphene/GaAs NIR photodetectors can be further improved, with the responsivity increased to 5 mA/W and rise/fall times decreased to 320/380 ns.

21.5.3 Graphene/Organic Semiconductors

Thanks to their simple solution processability at low temperatures [71], flexibility, low cost, and lightweight, organic semiconductors have attracted great interest in forming heterojunctions with graphene for photodetector applications. As shown in Fig. 21.9, a graphene/pentacene heterostructure can be fabricated on flexible substrates to serve as a multifunctional photodetection with nonvolatile memory function for storing optical signals [72]. The device exhibits excel-

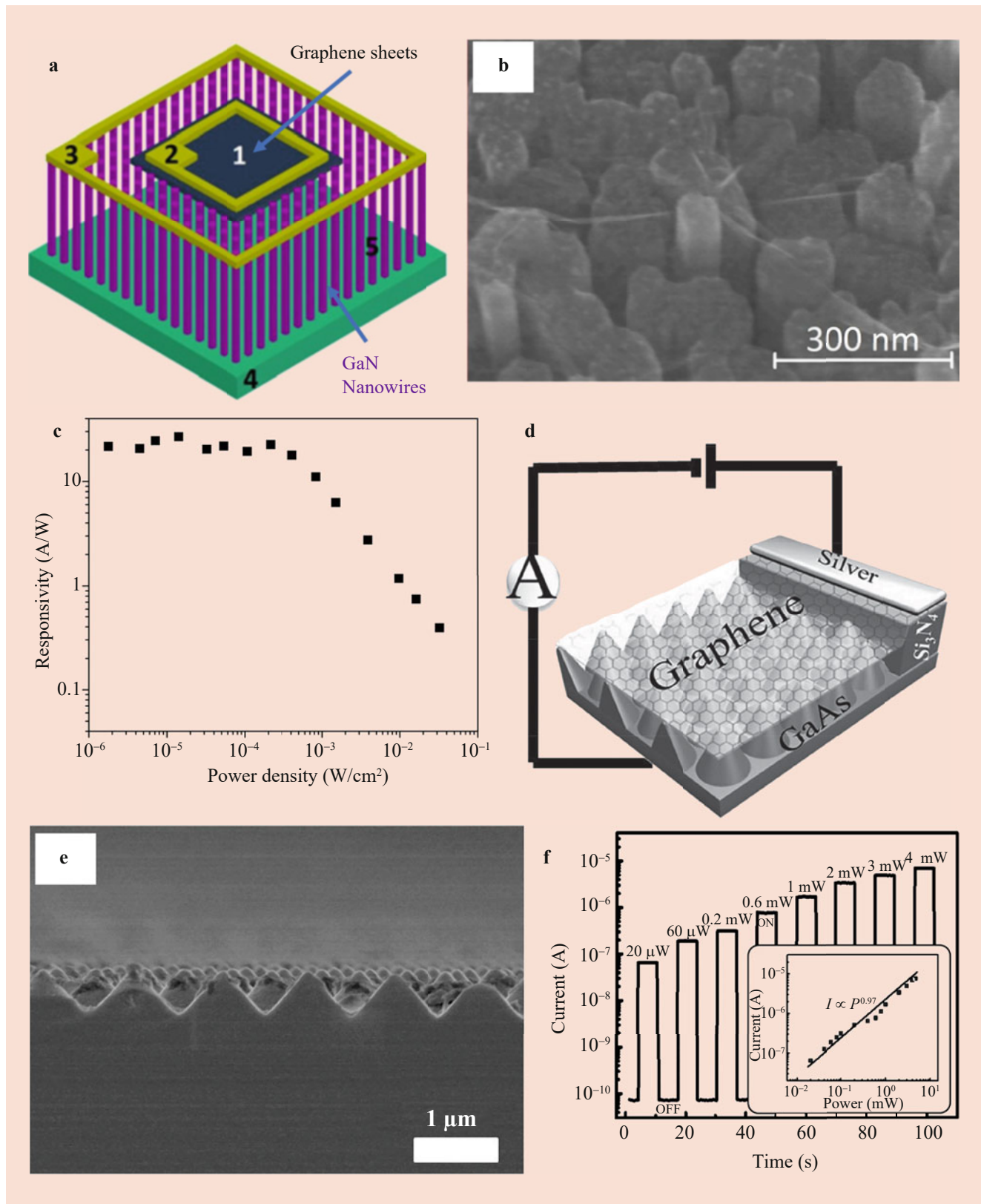


Fig. 21.8 Photodetectors based on graphene/III–V semiconductor heterostructures. (a) Schematic of a photodetector based on GaN nanowire array covered by graphene sheet. The yellow parts are electrodes. (b) Scanning electron microscopy (SEM) image of a graphene film on GaN nanowires [67]. (c) Responsivity for various incident power densities. (d) Schematic of a graphene/GaAs nanocone array photodetector [68].

(e) A typical cross-sectional SEM image of the n-GaAs nanocone array after etching. (f) Photoresponse of the graphene/GaAs nanocone array photodetector under various light intensities. Inset: the fitting of the relationship between the photocurrent and light intensity. (Adapted with permission from [67] Copyright (2013) AIP Publishing for a–c and from [68] Copyright (2014) John Wiley and Sons for d–f)

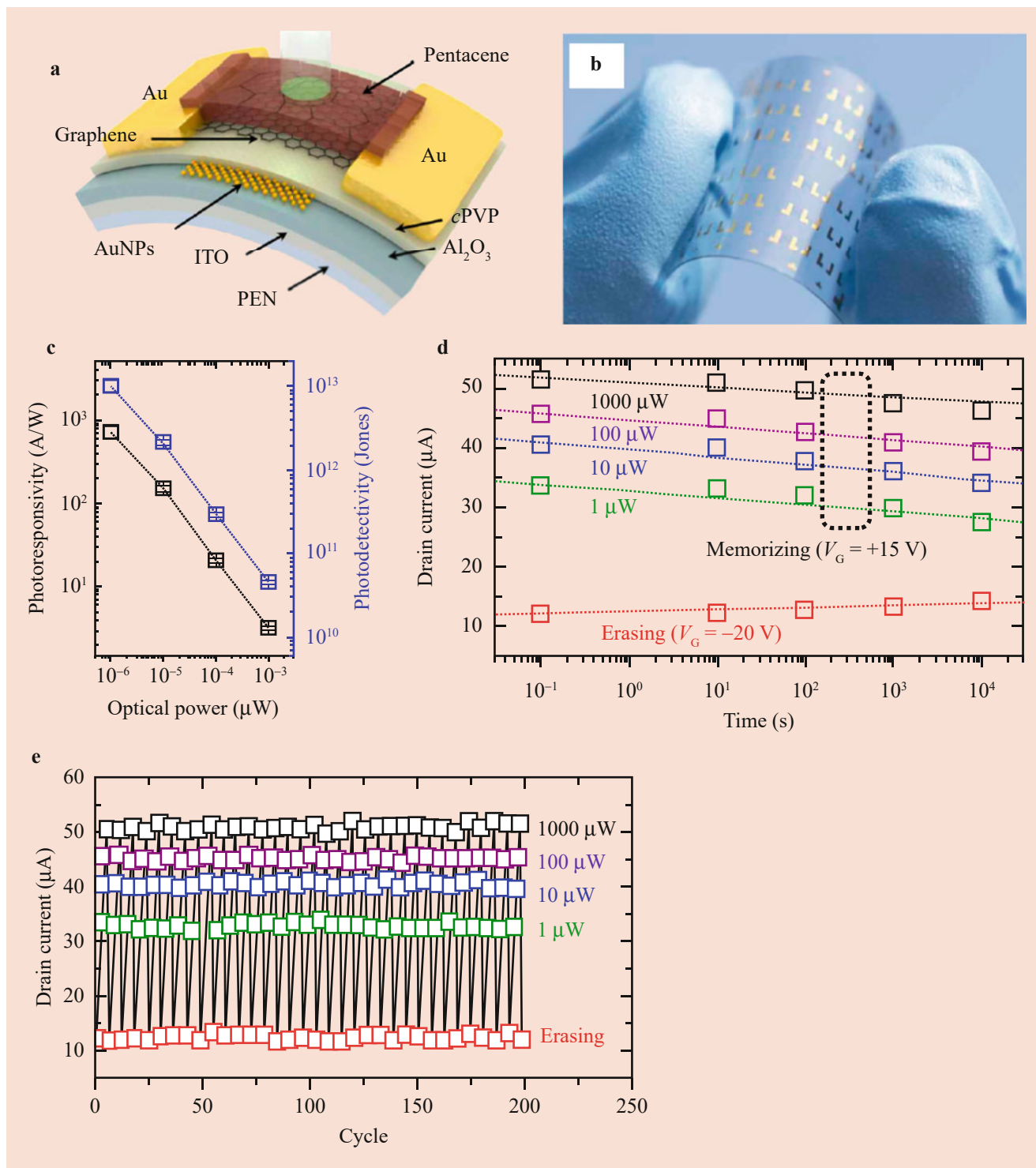


Fig. 21.9 Photodetectors based on graphene/organic semiconductor heterostructure. (a) Schematic of a graphene photodetector on flexible substrates with a pentacene light absorption layer and an Au nanoparticle charge trapping layer. (b) Photograph of the device. (c)

Responsivity and specific detectivity at different incident illumination power. (d) Retention time and (e) cycling test of the device with a memory functionality under various illumination powers. (Adapted with permission from [72] Copyright (2015) American Chemical Society)

lent performance at 400–800 nm with maximum responsivity and specific detectivity of 700 A/W and of 10^{13} Jones (Fig. 21.9c), respectively. It can also retain the photocurrent for a long time exceeding 10^4 s (Fig. 21.9d). The photocurrent remains invariant for more than 200 cycles and increases with the illumination power (Fig. 21.9e).

In addition, monolayer organic C8-BTBT crystals can also be integrated on graphene by van der Waals epitaxy [73] to obtain high-performance photodetectors with the responsivity larger than 10^4 A/W. By using multilayer C8-BTBT, the responsivity can be further increased to 4.76×10^5 A/W. The excellent performance may be attributed to the ultrahigh photoconductive gain and the high interfacial charge transfer efficiency due to the high quality of C8-BTBT layer and graphene/C8-BTBT interface [12]. However, the multilayer photodetection has much longer response time (~ 830 ms) than the monolayer device (~ 25 ms), probably due to the interlayer hopping of trapped carriers within the C8-BTBT crystals.

21.5.4 Graphene/Perovskites

Organic-inorganic halide perovskite materials are widely used in solar energy applications and recently have been envisioned as excellent candidate for next-generation photodetector materials because of their high adsorption coefficient, tunable bandgap, small exciton binding energy, long carrier diffusion length, ambipolar charge transport, and high carrier mobility [12]. It has been demonstrated that graphene/perovskites, such as graphene/ $\text{CH}_3\text{NH}_3\text{PbI}_3$ (MAPbI₃) hybrid, can achieve a responsivity of several hundreds of A/W at a response time shorter than 1 s [74, 75] (Fig. 21.10). The enhanced performance is mainly ascribed to the electron transfer from graphene to perovskite layer to fill its empty states in the valence band and hence reduce the photocarrier recombination. Furthermore, photodetectors based on vapor deposited ultra-flat MAPbI₃ films on graphene obtain an even higher responsivity of 1.73×10^7 A/W and specific detectivity of 2×10^{15} Jones [76]. In particular, when a thin layer of P3HT has been inserted between MAPbI_{3-x}Cl_x perovskite and graphene as a hole-transport layer [77], the carrier diffusion length is significantly increased, resulting in more efficient transfer of photogenerated holes to graphene and electrons to perovskite layer. Remarkably, a record value of 4.3×10^9 A/W has been obtained for the P3HT-enhanced photodetectors.

21.5.5 Graphene/Other 2D Materials

Besides graphene, black phosphorus (BP) and transition metal dichalcogenides (TMDCs) are also popular 2D layered

materials for optoelectronic applications [6]. BP is a direct bandgap semiconductor whose bandgap can be tuned from 0.3 to 1.9 eV by reducing the number of layers [78]. It excels in photodetection due to the easy excitation by absorption of visible and NIR lights [79]. Its anisotropic crystal structure and hence anisotropic electrical and optical properties lead to promising polarization-dependent light detection. Similarly, TMDCs, such as MoS₂, MoSe₂, WS₂, and WSe₂, also show tunable bandgaps ranging from an indirect bandgap of ~ 1.1 eV in bulk crystal to a direct energy gap of ~ 1.9 eV in monolayer crystal [80, 81]. For example, TMDCs could be used to manufacture photodetectors with high on/off ratio, which is superior to zero-bandgap graphene. Recently, several III–VI group layered (transition metal monochalcogenide) materials have also been demonstrated as promising photoresponse materials, such as GaS, GaSe, and InSe [6]. They also exhibit good tunability in bandgaps through adjusting the layer number. In addition to 2D semiconducting materials, 2D insulating materials also play an important role in photodetection. For example, hexagonal boron nitride (h-BN) are usually used as appealing barrier layer to restrain the dark current, due to its good chemical stability and thermal conductivity [82].

Although a large variety of individual 2D materials have demonstrated promising photodetection applications, the more attractive property of 2D materials for photodetectors relies on their van der Waals interaction between neighboring layers without dangling bonds, which enables the integration of multiple 2D materials to form heterostructures and obtain fundamentally different properties [12]. In a common geometry, 2D layered semiconductors and graphene act as the light absorber and the electrodes, respectively, to form planar metal-semiconductor-metal phototransistors. Different from metal electrodes, the Schottky barrier between the graphene electrode and the 2D semiconductors can be tuned by adjusting the Fermi level of graphene, making it possible to obtain ideal Ohmic contact between the two 2D materials. Also, the photoresponse characteristics of the heterostructures can be adjusted by electrostatic gating or optical input control [12]. Up to now, heterostructures between TMDC, BP, and III–VI 2D semiconductors have all been developed for photodetectors, as introduced below.

Various high-performance photodetectors based on graphene/TMDC heterostructures have been demonstrated with the TMDC being MoS₂, MoTe₂, WS₂, WSe₂, and so on. Remarkably, a high responsivity of up to 10^{10} A/W has been achieved in phototransistors based on heterostructures between mechanically exfoliated graphene and MoS₂ [85]. The high responsivity relies on the local trapping of photogenerated holes in MoS₂ and the gate electric field-enhanced electron transfer to graphene. The trapped holes can even act as local gates to generate significant photogating effect on graphene through capacitive coupling. Meanwhile,

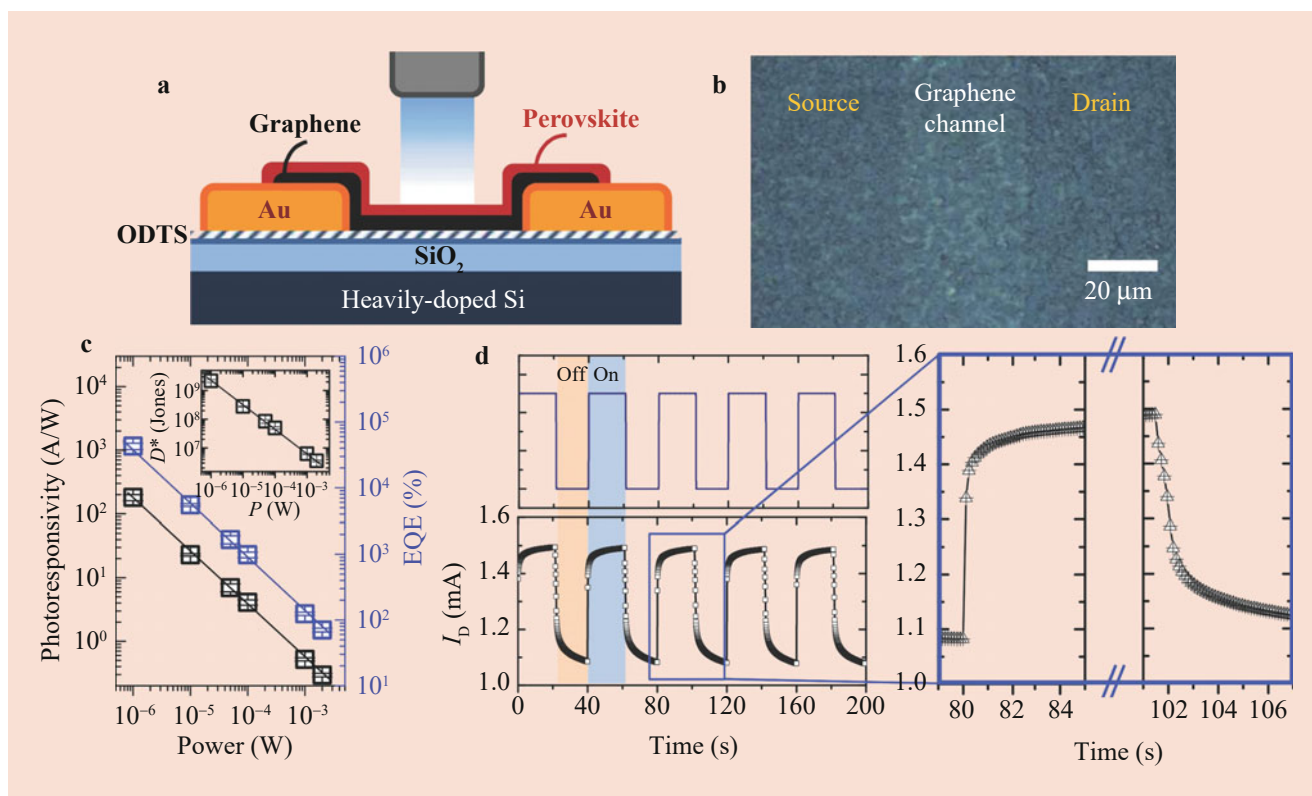


Fig. 21.10 Photodetectors based on graphene/perovskite heterostructures. (a) Schematic of the hybrid photodetector. (b) Optical micrograph of the $\text{CH}_3\text{NH}_3\text{PbI}_3$ -graphene photodetector. (c) Responsivity, EQE, and specific detectivity (inset) under different illumination powers. (d)

On-off switching characteristics of the photodetectors under alternative dark and light illuminations. (Adapted with permission from [74] Copyright (2014) John Wiley and Sons)

however, the trapped holes have long lifetime that evidently increase the response time of the photodetectors. In contrast, a graphene/ WSe_2 /graphene heterostructure [83] with a trilayer WSe_2 (2.2 nm thick) sandwiched between two graphene electrodes (Fig. 21.11a–c) exhibits fast response of around 5.5 ps and high internal quantum efficiency (70%). In another study, it is found that a graphene/ WS_2 /graphene heterostructure phototransistor shows abnormal dependence of the responsivity on incident light power [86]. The responsivity increases with the increasing optical power at a gate voltage of 0 V (off state), whereas it decreases at the gate voltage of 30 V (on state). The mechanism could be at on state; the photogating effect increases the Fermi level and reduces the contact resistance, so that the Fermi level of graphene is weakly influenced by illumination, thereby causing different power dependence of responsivity. Interestingly, a unique MoS_2 /graphene/ WSe_2 heterostructure-based photodetector (Fig. 21.11d–f) indicates the broadband response in the range from 400 to 2400 nm [84], with high responsivity and detectivity, respectively, of 10^4 A/W and 10^{15} Jones in the visible range, but decreasing to 0.1 A/W and 10^9 Jones at 2400 nm IR wavelength. The possible reason

for the performance dependence on the incident light wavelengths is that short-wavelength light can be absorbed by all the three materials (WSe_2 , graphene, and MoS_2) in the heterostructures, while long-wavelength light can only be absorbed by graphene which results in low photocurrents.

Recently, BP and III–VI 2D materials have also been integrated with graphene to fabricate wideband 2D heterostructure photodetectors. Highly efficient photodetectors operating at NIR wavelengths have been fabricated based on the graphene/BP heterostructures (Fig. 21.12) [87]. Thanks to the large photon absorption over a broadband wavelength range of the BP flakes, the graphene-BP heterostructure device exhibits a broadband photodetection from the visible to IR wavelengths and moreover shows a high responsivity up to $\sim 3.3 \times 10^3$ A/W at 1550 nm, which is more than 3000 times higher than those of previously reported photodetectors operating at the same wavelength. All the devices with different BP thickness exhibit qualitatively similar behaviors, while thicker BP flakes give rise to higher photoresponse (Fig. 21.12d). The devices can be stable for at least 60 days when operating at ambient conditions (Fig. 21.12e). They also show a high photoconductive gain (1.13×10^9), an ultrafast charge transfer (41 fs, Fig. 21.12f), a polarization-

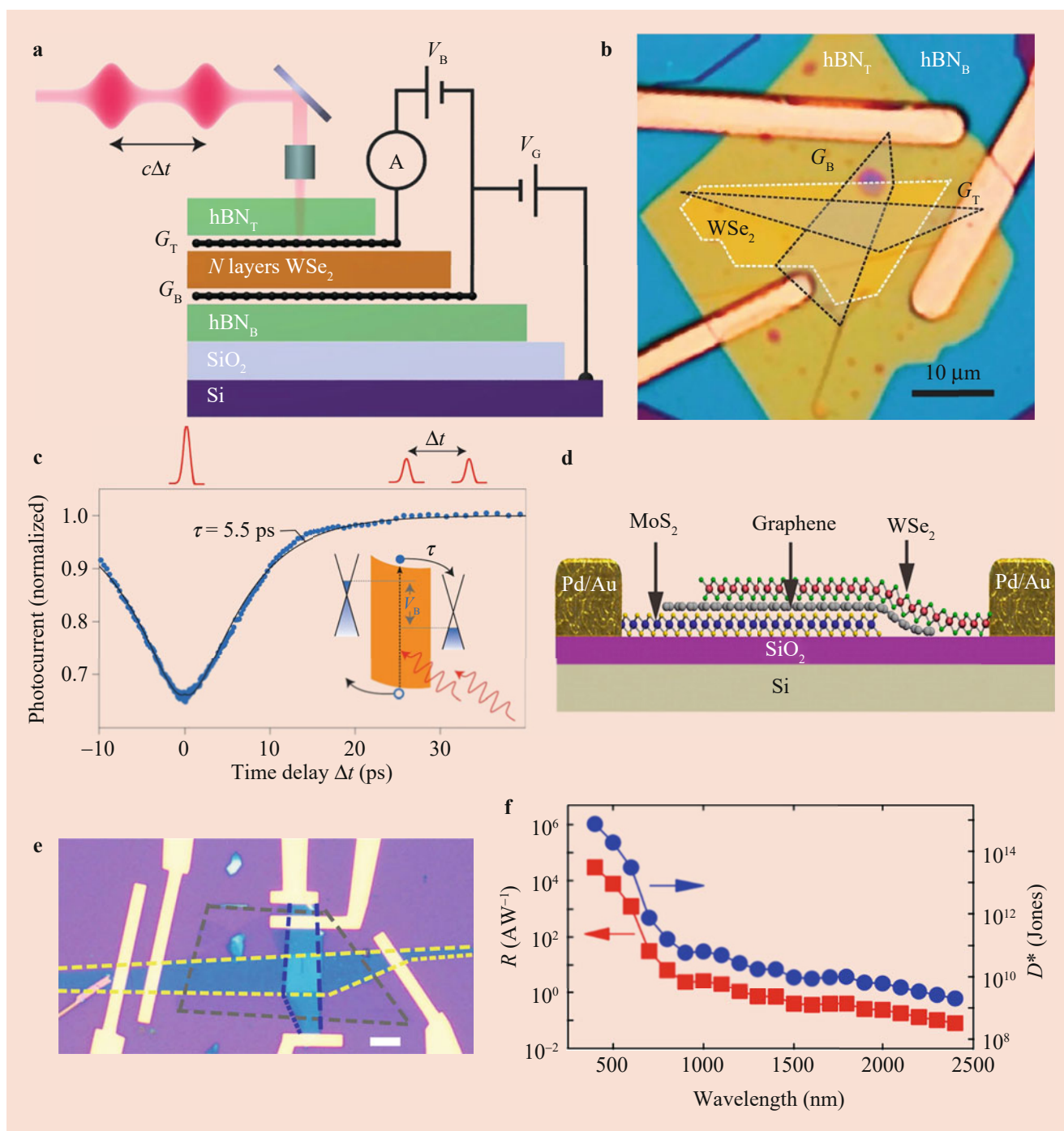


Fig. 21.11 Photodetectors based on graphene/TMDC heterostructures. (a) Schematic of a graphene/WSe₂/graphene heterostructure and the setup for detecting time-resolved photocurrent. Two ultrashort pulses, delayed by a controllable distance $c\Delta t$ (c is the speed of light), are focused on the device on a Si back gate to which a gate voltage (V_G) is applied between the top (G_T) and bottom (G_B) graphene layers to measure the photocurrent [83]. (b) Optical image of a heterostructure comprising a 2.2-nm-thick WSe₂ flake. The graphene and WSe₂ flakes

are outlined and shaded for clarity. (c) The dependence of photocurrent on the time delay between two pulses Δt . (d) Schematic of cross section and (e) photograph of top view of a photodetector based on MoS₂/graphene/WSe₂ heterostructures [84]. (f) The dependence of responsivity and detectivity of the devices in (d) under different incident light wavelength. (Adapted with permission from [83] Copyright (2015) Springer Nature for a–c, and from [84] Copyright (2016) American Chemical Society for d–f)

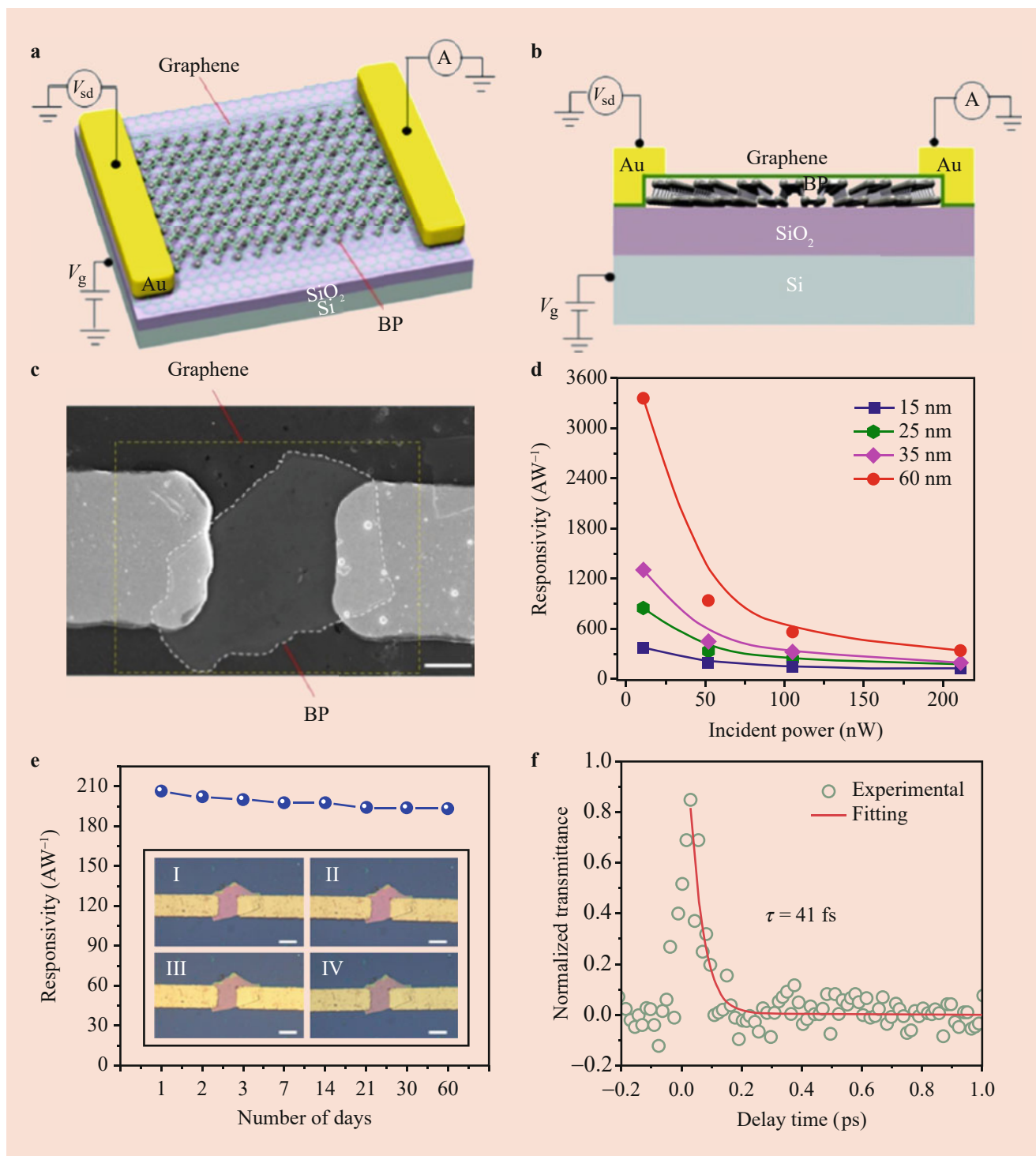


Fig. 21.12 A photodetector based on graphene/BP heterostructure. (a) 3D schematic and (b) schematic of cross-section view of the device. (c) SEM image of the graphene/BP heterostructured photodetector. Scale bar: 2 μm . (d) Responsivity as a function of incident power for different BP thickness. (e) Responsivity of a device under different

exposure time. Inset: from I to IV, the exposure times are 1 day, 7 days, 30 days, and 60 days, respectively. Scale bars: 8 μm . (f) Measured transmittivity transients of graphene/BP heterostructure at 1550 nm with an average pump power of 800 μW . (Reprinted with permission from [87] Copyright (2017) American Chemical Society)

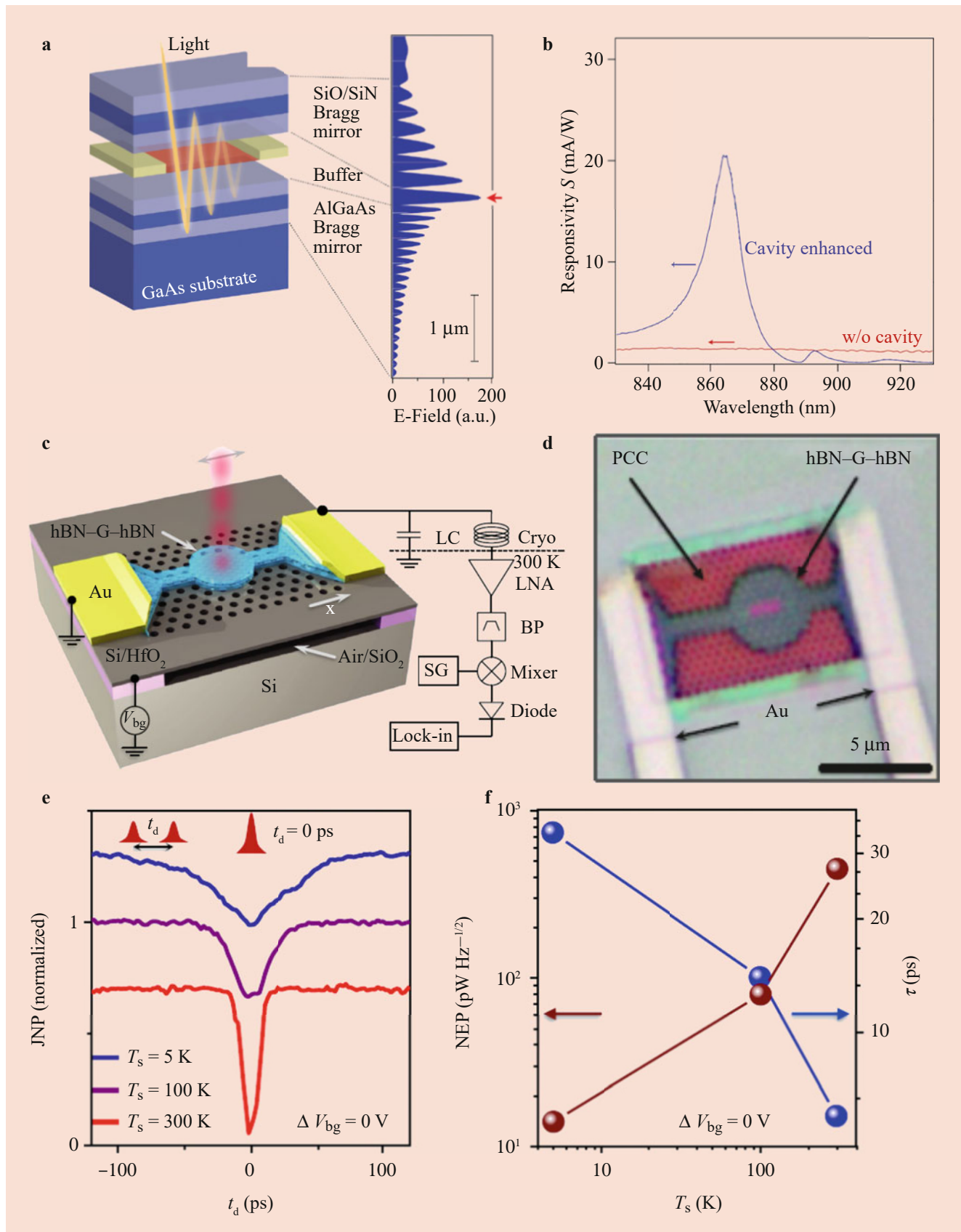


Fig. 21.13 (continued)

dependent photocurrent response, and a long-term stability at 1550 nm [87]. In another study, by using the broadband transparency of graphene and the favorable band lineup of graphene with InSe, wideband photodetectors with spectral response extending from NIR to visible spectrum have been fabricated based on planar graphene/n-InSe/graphene van der Waals heterostructures. The devices exhibit high responsivity of up to 10^5 A/W at wavelength of 633 nm and fast rise/fall times of 1/10 ms [88]. The high responsivity appears in the vertically stacked InSe and graphene layers with an optical window created by overlapping the two graphene electrodes, thus enabling sensitive photodetection.

21.6 Integrated Graphene Photodetectors

The low absorption of monolayer graphene (only $\sim 2.3\%$ of incident light) severely limits the overall responsivity of conventional graphene photodetectors to a typical value of a few mA/W. Highly desired are techniques that can effectively improve the optical absorption and responsivity. It has been discussed in Sect. 21.5 that integration of graphene photodetectors with light absorbers (such as quantum dots and perovskite) can improve the responsivity through the photogating effect. But typically these techniques result in lower operating speed [54, 74]. In this section, we discuss about the techniques of integrating graphene photodetectors with optical cavity and waveguides to improve the device performance.

21.6.1 Integration with Optical Cavity

It has been demonstrated as an effective way to significantly improve light absorption through embedding graphene into optical or photonic crystal cavities (PCC) [10]. Typically, optical cavities comprise arranged mirrors (either Bragg mirrors or metallic reflectors) [89, 91] with the gap equal to a quarter of the resonant wavelength so as to trap the electric field inside the cavities. When graphene integrates with an optical cavity, light may pass through it for several times which significantly increases the light absorption. Furchi et al. [89] integrated a metal/graphene/metal detector with a Bragg mirror-based microcavity (Fig. 21.13a, b) to reach a light absorption of 60% (about 26-fold enhanced) and a

responsivity of 21 mA/W. However, it is worthy of mentioning that the sharp resonant peak of an optical cavity often reduces the operating bandwidth of photodetectors, because the Bragg mirror-induced optical confinement is only in the vertical direction [10]. In contrast, PCC permits very high-quality factor due to the three-dimensional optical confinement. Dmitri et al. [90] have demonstrated a proof-of-concept device (Fig. 21.13c, d) of a high-quality hBN/graphene/hBN heterostructure bolometer placed onto a suspended silicon PCC and integrated with a Johnson noise readout. The device operates at telecom wavelengths and exhibits an enhanced bolometric response at charge neutrality with a NEP about 10 pW Hz $^{-1/2}$ and a record fast thermal relaxation time <35 ps (Fig. 21.13e, f).

21.6.2 Integration with Waveguides

In addition, due to their very low losses and high optical mode confinement, silicon waveguides have enabled a large variety of new applications, including nano-optomechanics, biosensing, nonlinear optics, and very long-wavelength integrated photonics [96]. It has also allowed hybrid integration of new materials into the silicon system for extended functionality, for example, integrating organic materials to increase optical nonlinearities and bonding III–V materials to create on-chip light sources. Integration of graphene photodetectors with low-loss optical waveguides can also greatly enhance the light absorption. The waveguides confine and guide the evanescent mode of optical electric field which propagates parallel to graphene channels. Therefore, light interacts with graphene throughout its travel in the waveguide so as to maximize the optical absorption [10]. It has been demonstrated the light absorption of a graphene-integrated silicon waveguide based on a Mach-Zender interferometer [97] can be increased up to 50% and 90% in 15- μ m- and 50- μ m-long graphene samples, respectively. The responsivity is also increased to 0.05 A/W and 0.1 A/W for 24- μ m- [98] and 50- μ m [99]-long silicon waveguides, respectively. In particular, a high responsivity of 0.13 A/W is obtained (Fig. 21.14a) when a graphene/silicon heterostructure is naturally integrated with silicon waveguide on SOI substrate [92]. Also, a compact photodetector [95] is realized through embedding graphene *inside the slot layer* of high- k (Al_2O_3)

Fig. 21.13 Graphene-based photodetectors integrated with optical cavity. (a) (Left) Schematic drawing of a graphene microcavity photodetector, including a bottom Bragg mirror made from multiple periods weakly doped, alternating AlAs and $\text{Al}_{0.10}\text{Ga}_{0.90}\text{As}$ layers, a buffer layer of Si_3N_4 to maximize the electric field at the graphene sheet, the graphene layer (the graphene sheet is shown in red, and the metal contacts are in yellow), and a top Bragg mirror of $\text{SiO}_2/\text{Si}_3\text{N}_4$ layer. (Right) Electric field amplitude inside the cavity. (b) Comparison of responsivity of the bilayer graphene photodetectors with and without

cavity [89]. (c) Schematic and (d) optical micrograph of a graphene bolometer on top of a suspended silicon photonic crystal cavity and a Johnson noise readout. (e) Normalized Johnson noise power probed with two laser pulses (delayed with time t_d) at different device temperature T_s and (f) NEP and thermal relaxation time (τ) of the graphene bolometer in (c, d). (Adapted with permission from [89] Copyright (2012) American Chemistry Society (<https://pubs.acs.org/doi/10.1021/nl204512x>), further permission should be directed to ACS) for a, b and from [90] Copyright (2018) Springer Nature for c–f)

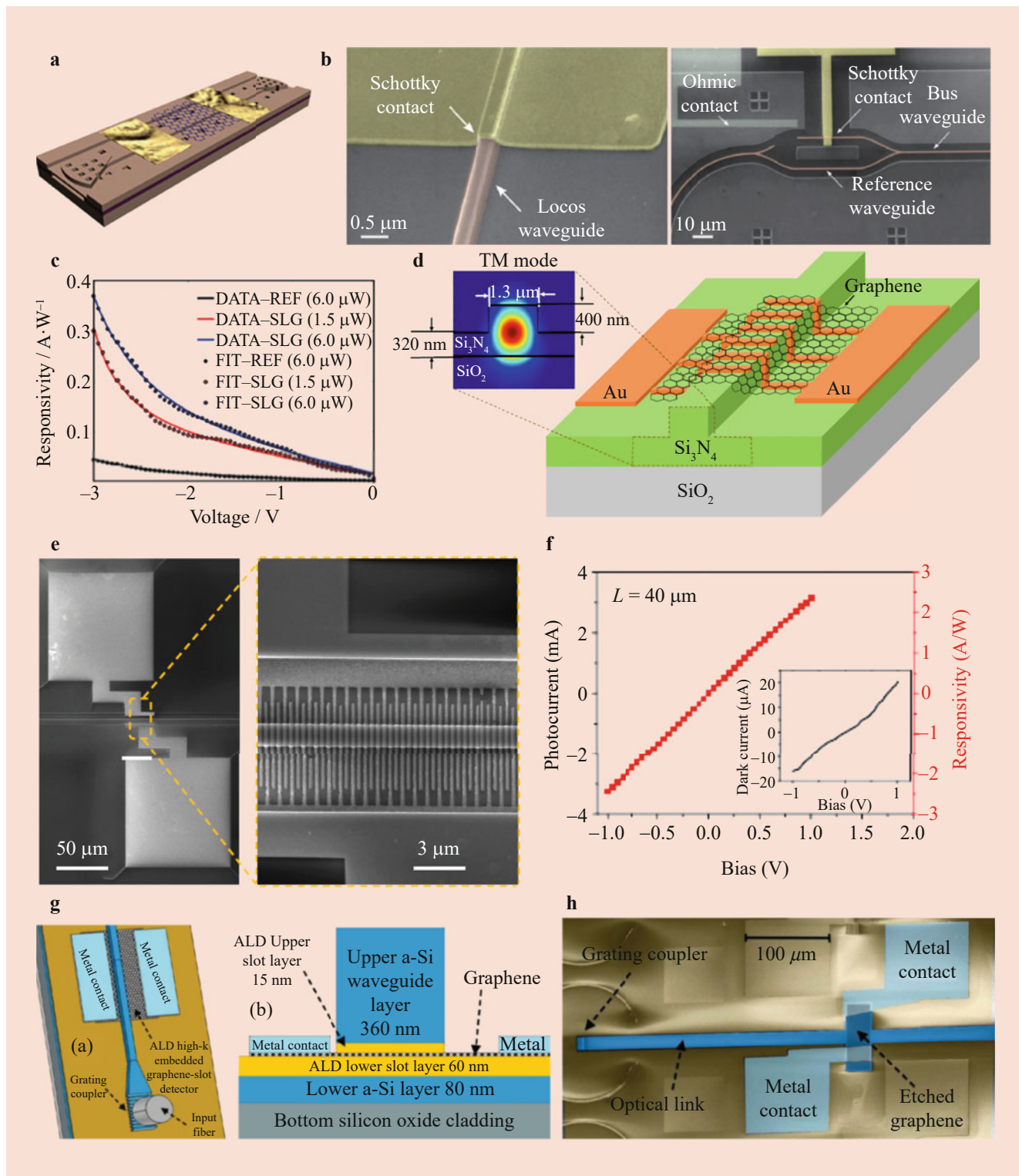


Fig. 21.14 Graphene photodetectors integrated with waveguides. **(a)** Schematic of graphene/silicon heterostructure waveguide photodetector on an SOI waveguide [92]. **(b)** SEM images of a graphene silicon Schottky photodetector: (left) graphene is coupled to a waveguide and (right) layout of the complete device [93]. **(c)** Responsivity of device in **(b)**. **(d)** Schematic of a graphene-on-Si₃N₄ waveguide photodetector with transverse-magnetic (TM) mode distribution [94]. **(e)** SEM images of a fabricated photodetector before graphene transfer. **(f)** Photocurrent and responsivity as a function of bias with an input optical power of 1.314 mW to a photodetector with Si₃N₄ waveguide. Inset: dark current

against bias. **(g)** Schematics of photodetectors with embedded graphene in the slot of Al₂O₃ waveguide (left, top view; right, cross section). **(h)** SEM image of the photodetector with integrated waveguide. (Adapted with permission from [92] Copyright (2013) Springer Nature for **a**, from [93] Copyright (2016) American Chemistry Society (<https://pubs.acs.org/doi/10.1021/acs.nanolett.5b05216>, further permission should be directed to ACS) for **b**, **c**, from [94] Copyright (2018) AIP Publishing for **d–f**, and from [95] Copyright (2014) IEEE Proceedings for **g**, **h**)

slot waveguides (Fig. 21.14). Due to the high mode concentration in the slot region, this structure leads to a high light-graphene interaction and hence a responsivity of 3.6 mA/W for a 40- μm -long graphene detector. Making use of the avalanche multiplication at high reverse biases of an integrated graphene/silicon Schottky photodetector (Fig. 21.14b, c), a high responsivity up to 0.37 A/W is achieved for 1.5 μm incident light [93]. A recent study [94] also demonstrated that graphene photodetectors integrated on silicon nitride waveguides (Fig. 21.14d–f) with interdigitated metal contacts (to reduce the channel spacing down to ~ 200 nm) exhibit a high responsivity of 2.36 A/W and bandwidth of 33 GHz at 1550 nm.

21.7 Graphene Photodetectors with Special Geometry or Architectures

Recently, it has been demonstrated that special geometry and architectures have potential to lead to new mechanism and functionalities of graphene-based photodetectors.

Despite the diversity of mechanisms in graphene-based photodetectors, such as PV and PTE effects, all of these photocurrents are prominent at high charge densities but are suppressed at the charge neutrality point (CNP). A recent research [100] has discovered a new photocurrent phenomenon in graphene that appears exclusively when the Fermi level is at the Dirac point and vanishes at high charge densities. For intrinsic graphene with special geometrical patterns, such as those in Fig. 21.15, the photocurrents emerge at free graphene edges (in area far away from the contacts) exclusively at the CNP where the Fermi level matches the Dirac point. At high charge densities where the Fermi level leaves away from the Dirac point, conventional photocurrents appear only near the graphene/metal contacts. The new mechanism originates in the asymmetry of electron-hole velocities in graphene [101]. Electrons and holes have an intrinsic velocity difference, and upon being excited by photons, they will diffuse at different speeds, separate, and produce a local electric field. Since the diffusion has no directional preference, the local electric fields are circularly symmetric around the excitation point and cancel each other out, resulting in zero total electric field in the electrical circuit. However, when light is shone on the edge of the graphene, the diffusion is no longer circularly symmetric, and this gives rise to a residual electric field to produce photocurrent in the circuit. Therefore, graphene with well-designed edges can serve as a photocurrent source [101]. As the CNP photocurrents are carried at the group velocity of unthermalized electrons, they should exhibit an ultrafast response time, possibly leading to ballistic photodetectors. Hence, the new mechanism is promising for ultrahigh-speed and ultra-broadband optoelectronics [100].

The attractive properties of graphene and 2D materials for photodetectors are not restricted to their unique electrical and optical properties, but also include their mechanical strength and flexibility and great compatibility with various substrates. For example, making use of heterostructure of single-layer graphene and MoS_2 , Domenico et al. [103] developed flexible photodetectors on plastic substrates for visible wavelengths. The devices are gated by polymer electrolyte with external responsivity up to ~ 45.5 A/W (at least two orders of magnitude higher than that of conventional semiconductor membranes), photoconductive gain $\sim 4 \times 10^5$, operation voltage < 1 V, and optical transparency $> 82\%$. In addition, Wonho et al. [102] even integrate an array of graphene/ MoS_2 heterostructures on 3D substrates with complex and mechanically assembled 3D systems (Fig. 21.16). The 3D photodetectors exhibit a maximum responsivity of 38 A/W and rise and decay time of 290 ± 130 ms and 420 ± 210 ms, respectively. In particular, the overall photodetectors are optically transparent ($\sim 87\%$ transmittance at 550 nm) which enables 3D systems to simultaneously detect the position, direction, intensity, and angular divergence properties of incident light. To realize the same functionality in 2D layouts, significantly more components are needed [102].

21.8 Conclusions and Outlook

The performance of representative graphene-based photodetectors is summarized in Table 21.1.

From Table 21.1, one may readily find that graphene-based photodetectors are being developed with intensive efforts from extensive research fields. So far, the focus is still on the performance improvement through integration with various materials, components, and systems. For many types of detectors, their performance has already surpassed the existing technologies, such as high responsivity (up to $\sim 10^{10}$ A/W), wideband detection (UV-THz), and ultrafast response speed (down to ps). This can also be clearly seen in Fig. 21.17 which indicates a systematic comparison of performance metrics between standard and graphene (or 2D materials-)-based photodetector technologies [4]. Undoubtedly, graphene-based photodetectors have great potential to complement to or even replace the present silicon photodetectors in many applications. However, it should be mentioned that most techniques still make trade-off between different performance metrics. For example, heterostructures typically give rise to high responsivity, while the response speed is sacrificed. Integration with optical cavity increases the light absorption but significantly limits the operating bandwidth. So highly desired are comprehensive technologies that may integrate multiple complementary materials (especially new 2D materials) and components (especially optical cavity and waveguides)

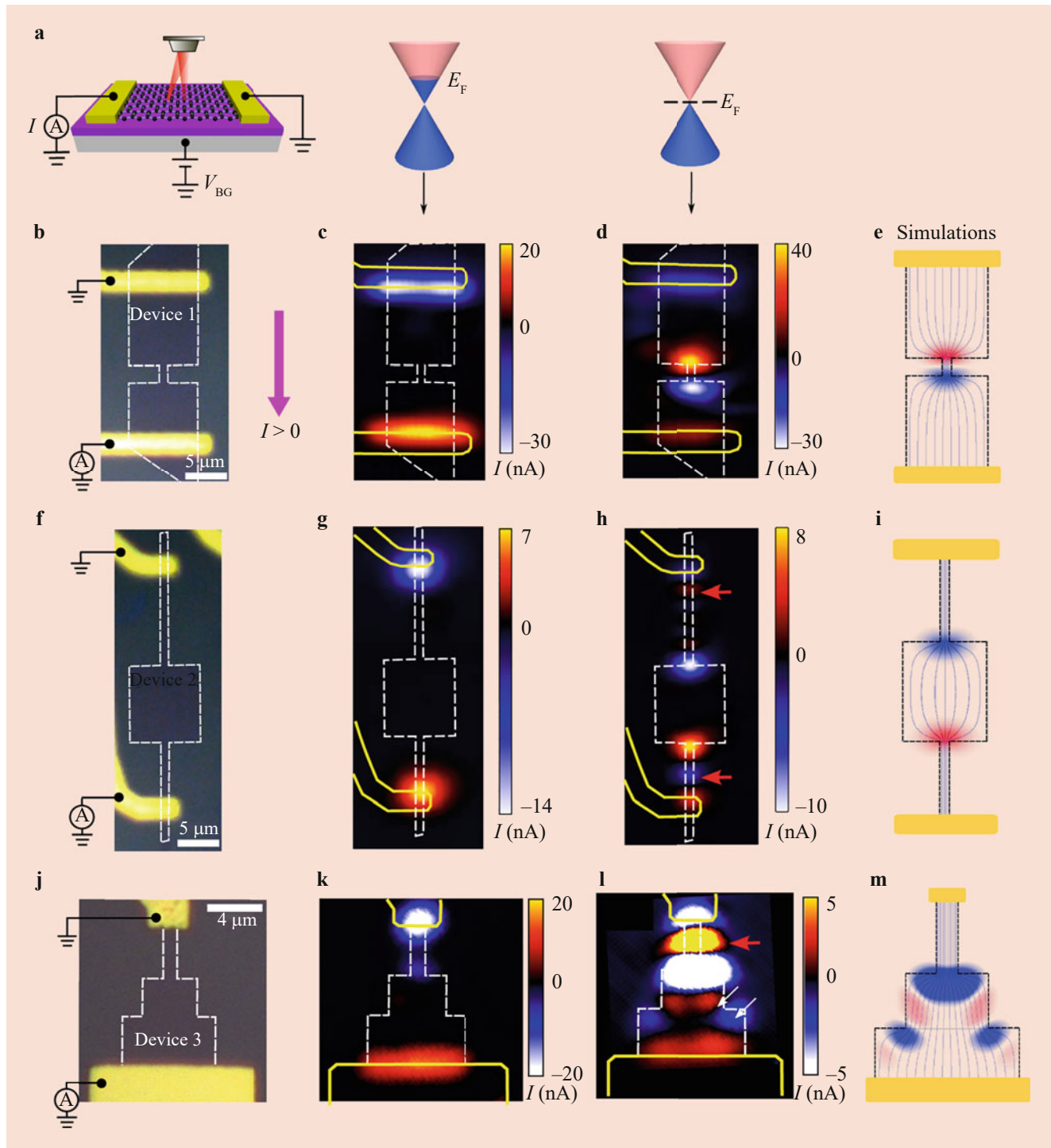


Fig. 21.15 Intrinsic long-range edge photocurrent in charge-neutral graphene with different geometries. (a) Schematic of a back-gated graphene device with scanning laser excitation. (b–d) Optical image (b) and scanning photocurrent images (c, d) of Device 1 with a narrower middle graphene channel. At high charge density (c), the photocurrent is mainly generated at the contact areas, whereas at the CNP (d) significant photocurrent occurs at the two ends of the middle graphene region. (e)

Simulation of the photocurrent image for Device 1. (f–i) Similar figures to (b–e) for Device 2 with a wider middle graphene section. (j–m) Similar figures to (b–e) for Device 3 with three rectangular graphene regions with increasing widths. The white arrows in (l) indicate that the photocurrent is generated from the graphene edge. The red arrows in (h) and (l) denote the photocurrent along the straight edges. (Reproduced with permission from [100] Copyright (2018) Springer Nature)

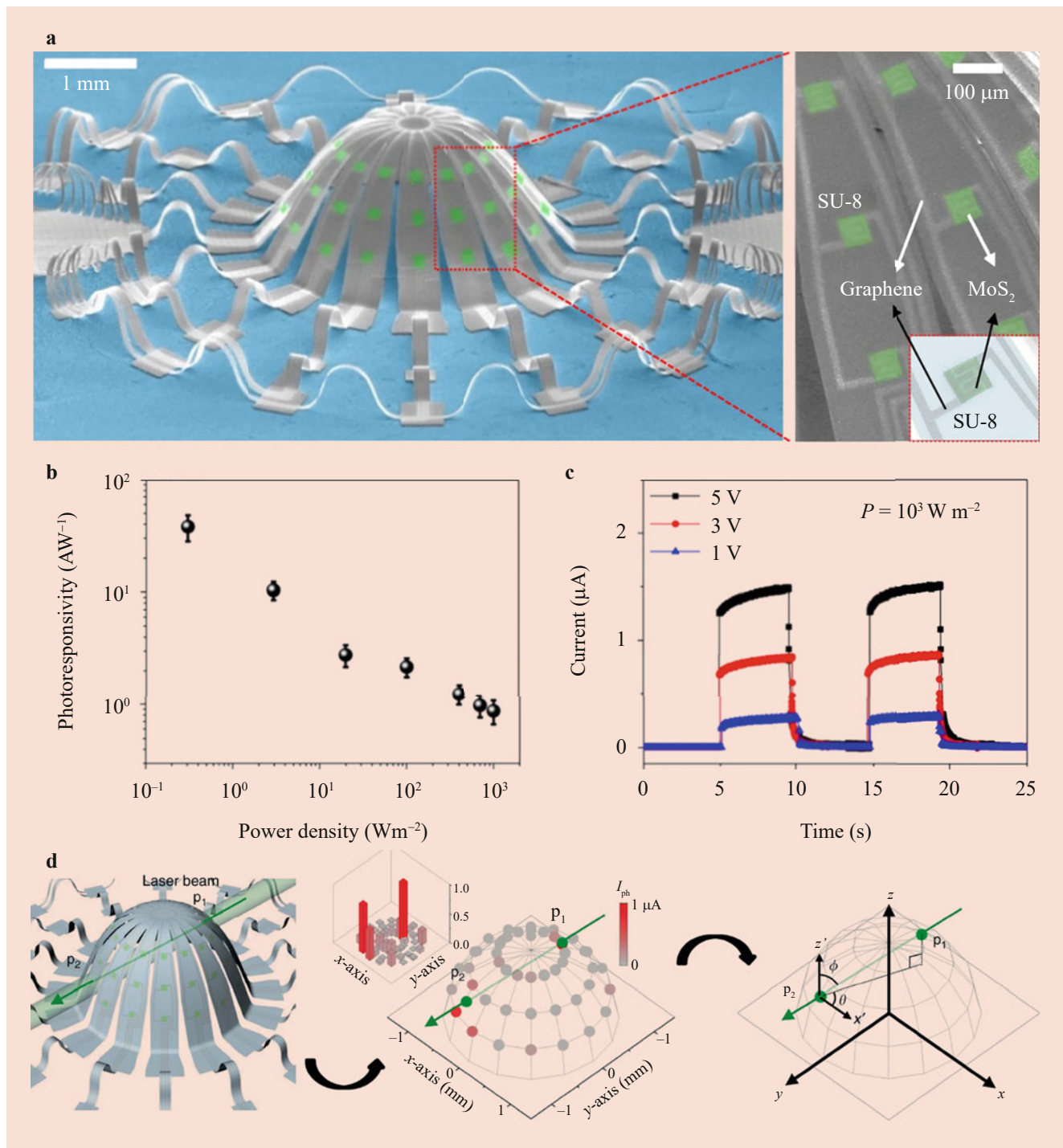


Fig. 21.16 Graphene/MoS₂ photodetectors on 3D hemispherical structure. **(a)** Colorized SEM image of photodetectors consisting of MoS₂ (green), graphene (light gray), and SU-8 (gray) on the hemisphere with 3D interconnects. **(b)** Responsivity of the photodetector at a bias voltage of 3 V for different laser power densities. **(c)** Time-resolved photoresponses of the devices under laser illumination at different power densities. **(d)** Operating principle of 3D photodetection: (left)

penetration of the laser beam at two points of the 3D hemispherical surface, (middle) photocurrent distribution on the hemisphere surface in the scenario, and (right) principle of estimating the incident direction of the laser from the photocurrent map. (Adapted with permission from [102] Copyright (2018) Springer Nature under the terms of the Creative Commons CC BY 4.0 license)

Table 21.1 Performance of graphene-based photodetectors

Device structure	Mechanism	Responsivity R_{ph} (A W ⁻¹)	Noise equivalent power NEP (W Hz ^{-1/2})	Detectivity D^* (Jones)	Response time (s)	References
Metal/graphene/ metal	Photovoltaic (PV)	6.1×10^{-3}				[9]
Dual-gated bilayer graphene	Bolometric	2×10^5 V W ⁻¹	3.3×10^{-14}		$\sim 1 \times 10^{-10}$	[40]
Antenna on SLG with back gate	Plasmon induced doping	1×10^{-2}			$\sim 2 \times 10^{-6}$	[48]
Graphene-PbS quantum dots hybrid with back gate	Photogating	$\sim 10^7$	$\sim 10^{-17}$ W (at $0.1 \Omega \text{ Hz}^{-1/2}$)	7×10^{13}	$\sim 10^{-6}$	[54]
Graphene/SiO ₂ /Si	PV, heterostructure	0.3				[59]
Graphene/SiO ₂ /Si (interdigitated)	PV, heterostructure	0.6				[60]
Ag nanoparticle/ graphene/porous Si	Plasmon, heterostructure	0.3			$\sim 3 \times 10^{-6}$	[65]
Au nanoparticle/ graphene/Si nanowire	Plasmon, heterostructure	1.5		2.5×10^{14}	$\sim 7 \times 10^{-5}$	[66]
Graphene/GaN NWs	PV, heterostructure	25				[67]
Graphene/pentacene	Hybrid	700		10^{13}		[72]
Graphene/C8-BTBT	Hybrid	1.6×10^4			2.5×10^{-2}	[73]
Graphene/MAPbI ₃	Hybrid	1.7×10^7		2×10^{15}	0.9	[76]
Graphene/P3HT/ MAPbI _{3-x} Cl _x	Hybrid	4.3×10^9			10	[77]
Graphene/WSe ₂ / graphene	Heterostructure	2×10^{-2}	5×10^{-12}		5.5×10^{-12}	[83]
Graphene/MoS ₂	Heterostructure	1×10^{10} at 130 K; 5×10^8 at room temperature				[85]
MoS ₂ /graphene/ WSe ₂	Heterostructure	10^4		10^{15}	5×10^{-5}	[84]
Graphene/BP	Heterostructure	3.3×10^3			5×10^{-3}	[87]
Graphene/n-InSe/ graphene	Heterostructure	10^5			10^{-3}	[88]
Microcavity- integrated graphene	Cavity-enhanced	2.1×10^{-2}				[89]
hBN/graphene/hBN with silicon PCC	Cavity-enhanced		10^{-11}		3.5×10^{-11}	[90]
Graphene/Si with Si waveguide	Heterostructure, waveguide- enhanced	0.13				[92]
Graphene/Si with Al ₂ O ₃ waveguide	Heterostructure, waveguide- enhanced	3.6×10^{-3}				[95]
Graphene/Si with Si ₃ N ₄ waveguide	Heterostructure, waveguide- enhanced	2.36	3.3×10^{-12}		1.2×10^{-12}	[94]
Pristine graphene with special geometry	Geometry-induced	1×10^{-3}			2.5×10^{-13}	[100]
Graphene/MoS ₂ on 3D substrates	Heterostructure	38			0.3	[102]

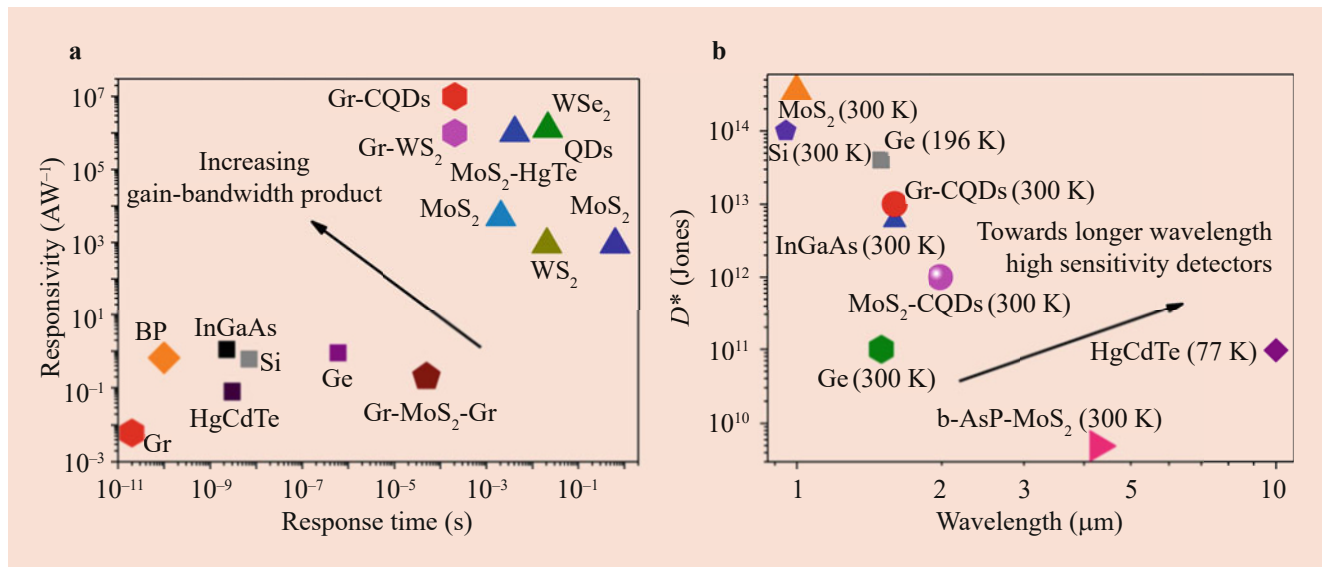


Fig. 21.17 Overview of performance metrics of standard and 2D-based photodetector technologies. (a) Responsivity against time response for various photodetector technologies. The top left region corresponds to high-gain bandwidth product detectors and should be the ultimate performance target of future photodetectors. (b) Plot of the

specific detectivity D^* against absorption onset (bandgap) for various photodetector technologies. “Gr” means graphene. (Reproduced with permission from [4] Copyright (2018) Springer Nature under the terms of the Creative Commons CC BY 4.0 license)

with graphene to achieve thorough improvement of various performance metrics. Moreover, the exploration of new mechanisms, such as the geometry-dependent photoresponse in graphene [100], may offer opportunities to provide innovative solutions for groundbreaking performance to essentially eliminate the present dilemma in making trade-off among different performance metrics.

Besides the competitive photodetection performance, graphene-based photodetectors excel in compatible form factor with the standard silicon technology and ideal adaptability to a large variety of substrates, either rigid or flexible, single crystalline or amorphous, and planar or 3D curved. This greatly simplifies the integration and offers opportunities to develop multifunctional photodetectors to enable engineering unique system-level function through simple integration of devices on desired substrates. A good example is shown in [102]. Therefore, one may expect more advanced photodetecting systems based on graphene photodetectors can be developed in the near future to provide both high performance and multifunctionalities.

Finally, it is worthy of emphasizing that the most attractive points of graphene and other 2D materials for photodetector applications do rely not only on their outstanding photonic performance but also on their unique combination of many other properties. It is important to make use of the latter to develop in the future advanced photodetectors that integrate multiple functionalities and merits. For example, most 2D materials are compatible with liquid solution processes, which offer opportunities to develop solution-processed or solution-printed photodetectors based on 2D materials [3,

104] for both performance- and cost-competitive technology [4]. On the other hand, distinguishingly different sensors can be produced even when graphene is placed in the same device structure. For instance, a suspended graphene with simply contacted source and drain contacts can be both a good photodetector with increased responsivity [27] and an excellent pressure sensor with orders of magnitudes higher sensitivity than conventional pressure sensors [105]. Consequently, it is becoming a new trend to develop multifunctional graphene sensors which after integrating with decoupling techniques can detect both light illuminance and other environmental signs, so as to provide a compact solution to comprehensive systems (e.g., environmental monitoring, energy management, health care, feedback control of machines) where various types of sensors are normally needed [72, 106]. A final observation is that most of the above detector types, how promising they may all be, depend on reliable, reproducible, and cost-effective fabrication technologies which, at the moment, still are to be shown for large-scale production.

References

1. Koppens, F.H., Mueller, T., Avouris, P., Ferrari, A.C., Vitiello, M.S., Polini, M.: Photodetectors based on graphene, other two-dimensional materials and hybrid systems. *Nat. Nanotechnol.* **9**, 780–793 (2014)
2. Hochberg, M., Baehr-Jones, T.: Towards fabless silicon photonics. *Nat. Photonics.* **4**, 492–494 (2010)
3. de Arquer, F.P.G., Armin, A., Meredith, P., Sargent, E.H.: Solution-processed semiconductors for next-generation photodetectors. *Nat. Rev. Mat.* **2**, 16100 (2017)

4. Konstantatos, G.: Current status and technological Prospect of photodetectors based on two-dimensional materials. *Nat. Commun.* **9**, 5266 (2018)
5. Jalali, B., Fathpour, S.: Silicon photonics. *J. Lightwave Technol.* **24**, 4600–4615 (2006)
6. Wang, G., Zhang, Y., You, C., Liu, B., Yang, Y., Li, H., Cui, A., Liu, D., Yan, H.: Two dimensional materials based photodetectors. *Infrared Phys. Technol.* **88**, 149–173 (2018)
7. Nair, R.R., Blake, P., Grigorenko, A.N., Novoselov, K.S., Booth, T.J., Stauber, T., Peres, N.M., Geim, A.K.: Fine structure constant defines visual transparency of graphene. *Science*. **320**, 1308 (2008)
8. Xia, F., Mueller, T., Lin, Y.-M., Valdes-Garcia, A., Avouris, P.: Ultrafast graphene photodetector. *Nat. Nanotechnol.* **4**, 839–843 (2009)
9. Mueller, T., Xia, F., Avouris, P.: Graphene photodetectors for high-speed optical communications. *Nat. Photonics*. **4**, 297–301 (2010)
10. Wang, X., Gan, X.: Graphene integrated photodetectors and optoelectronic devices – a review. *Chinese Phys. B*. **26**, 034201 (2017)
11. Wang, J., Han, J., Chen, X., Wang, X.: Design strategies for two-dimensional material photodetectors to enhance device performance. *InfoMat*. **1**, 33–53 (2019)
12. Shin, D.H., Choi, S.H.: Graphene-based semiconductor Heterostructures for photodetectors. *Micromachines (Basel)*. **9**, 350 (2018)
13. Peters, E.C., Lee, E.J.H., Burghard, M., Kern, K.: Gate dependent photocurrents at a graphene P-N junction. *Appl. Phys. Lett.* **97** (2010)
14. Mueller, T., Xia, F., Freitag, M., Tsang, J., Avouris, P.: Role of contacts in graphene transistors: a scanning photocurrent study. *Phys. Rev. B*. **79**, 245430 (2009)
15. Farmer, D.B., Golizadeh-Mojarad, R., Perebeinos, V., Lin, Y.M., Tulevski, G.S., Tsang, J.C., Avouris, P.: Chemical doping and electron-hole conduction asymmetry in graphene devices. *Nano Lett.* **9**, 388–392 (2009)
16. Lemme, M.C., Koppens, F.H., Falk, A.L., Rudner, M.S., Park, H., Levitov, L.S., Marcus, C.M.: Gate-activated Photoresponse in a graphene P-N junction. *Nano Lett.* **11**, 4134–4137 (2011)
17. Freitag, M., Low, T., Xia, F.N., Avouris, P.: Photoconductivity of biased graphene. *Nat. Photonics*. **7**, 53–59 (2013)
18. Brida, D., Tomadin, A., Manzoni, C., Kim, Y.J., Lombardo, A., Milana, S., Nair, R.R., Novoselov, K.S., Ferrari, A.C., Cerullo, G., Polini, M.: Ultrafast collinear scattering and carrier multiplication in graphene. *Nat. Commun.* **4**, 1987 (2013)
19. Malic, E., Winzer, T., Bobkin, E., Knorr, A.: Microscopic theory of absorption and ultrafast many-particle kinetics in graphene. *Phys. Rev. B*. **84** (2011)
20. Winzer, T., Knorr, A., Malic, E.: Carrier multiplication in graphene. *Nano Lett.* **10**, 4839–4843 (2010)
21. Tielrooij, K.J., Song, J.C.W., Jensen, S.A., Centeno, A., Pesquera, A., Zurutuza Elorza, A., Bonn, M., Levitov, L.S., Koppens, F.H.L.: Photoexcitation cascade and multiple hot-carrier generation in graphene. *Nat. Phys.* **9**, 248 (2013)
22. Gierz, I., Petersen, J.C., Mitrano, M., Cacho, C., Turcu, I.C., Springate, E., Stohr, A., Kohler, A., Starke, U., Cavalleri, A.: Snapshots of non-equilibrium Dirac carrier distributions in graphene. *Nat. Mater.* **12**, 1119–1124 (2013)
23. Johansson, J.C., Ulstrup, S., Cilento, F., Crepaldi, A., Zacchigna, M., Cacho, C., Turcu, I.C., Springate, E., Fromm, F., Raidel, C., Seyller, T., Parmigiani, F., Grioni, M., Hofmann, P.: Direct view of hot carrier dynamics in graphene. *Phys. Rev. Lett.* **111**, 027403 (2013)
24. Bistritzer, R., MacDonald, A.H.: Electronic cooling in graphene. *Phys. Rev. Lett.* **102**, 206410 (2009)
25. Tse, W.-K., Das Sarma, S.: Energy relaxation of hot Dirac fermions in graphene. *Phys. Rev. B*. **79** (2009)
26. Gabor, N.M., Song, J.C., Ma, Q., Nair, N.L., Taychatanapat, T., Watanabe, K., Taniguchi, T., Levitov, L.S., Jarillo-Herrero, P.: Hot carrier-assisted intrinsic Photoresponse in graphene. *Science*. **334**, 648–652 (2011)
27. Freitag, M., Low, T., Avouris, P.: Increased responsivity of suspended graphene photodetectors. *Nano Lett.* **13**, 1644–1648 (2013)
28. Dyakonov, M., Shur, M.: Shallow water analogy for a ballistic field effect transistor: new mechanism of plasma wave generation by dc current. *Phys. Rev. Lett.* **71**, 2465–2468 (1993)
29. Dyakonov, M., Shur, M.: Detection, mixing, and frequency multiplication of terahertz radiation by two-dimensional electronic fluid. *IEEE Trans. Electr. Devices*. **43**(380), 380–387 (1996)
30. Tomadin, A., Polini, M.: Theory of the plasma-wave Photoresponse of a gated graphene sheet. *Phys. Rev. B*. **88** (2013)
31. Vicarelli, L., Vitiello, M.S., Coquillat, D., Lombardo, A., Ferrari, A.C., Knap, W., Polini, M., Pellegrini, V., Tredicucci, A.: Graphene field-effect transistors as room-temperature terahertz detectors. *Nat. Mater.* **11**, 865–871 (2012)
32. Spirito, D., Coquillat, D., De Bonis, S.L., Lombardo, A., Bruna, M., Ferrari, A.C., Pellegrini, V., Tredicucci, A., Knap, W., Vitiello, M.S.: High performance bilayer-graphene terahertz detectors. *Appl. Phys. Lett.* **104**, 061111 (2014)
33. Park, J., Ahn, Y.H., Ruiz-Vargas, C.: Imaging of photocurrent generation and collection in single-layer graphene. *Nano Lett.* **9**, 1742–1746 (2009)
34. Lee, E.J., Balasubramanian, K., Weitz, R.T., Burghard, M., Kern, K.: Contact and edge effects in graphene devices. *Nat. Nanotechnol.* **3**, 486–490 (2008)
35. Xia, F., Mueller, T., Golizadeh-Mojarad, R., Freitag, M., Lin, Y.M., Tsang, J., Perebeinos, V., Avouris, P.: Photocurrent imaging and efficient photon detection in a graphene transistor. *Nano Lett.* **9**, 1039–1044 (2009)
36. Giovannetti, G., Khomyakov, P.A., Brocks, G., Karpan, V.M., van den Brink, J., Kelly, P.J.: Doping graphene with metal contacts. *Phys. Rev. Lett.* **101**, 026803 (2008)
37. Huard, B., Stander, N., Sulpizio, J.A., Goldhaber-Gordon, D.: Evidence of the role of contacts on the observed electron-hole asymmetry in graphene. *Phys. Rev. B*. **78** (2008)
38. Urich, A., Pospischil, A., Furchi, M.M., Dietze, D., Unterrainer, K., Mueller, T.: Silver Nanoisland enhanced Raman interaction in graphene. *Appl. Phys. Lett.* **101**, 153113 (2012)
39. Xu, X., Gabor, N.M., Alden, J.S., van der Zande, A.M., McEuen, P.L.: Photo-thermoelectric effect at a graphene Interface junction. *Nano Lett.* **10**, 562–566 (2010)
40. Yan, J., Kim, M.H., Elle, J.A., Sushkov, A.B., Jenkins, G.S., Milchberg, H.M., Fuhrer, M.S., Drew, H.D.: Dual-gated bilayer graphene hot-electron bolometer. *Nat. Nanotechnol.* **7**, 472–478 (2012)
41. Tan, Y.W., Zhang, Y., Stormer, H.L., Kim, P.: Temperature dependent electron transport in graphene. *Eur. Phys. J. Spec. Topics*. **148**(15), 15–18 (2007)
42. Han, Q., Gao, T., Zhang, R., Chen, Y., Chen, J., Liu, G., Zhang, Y., Liu, Z., Wu, X., Yu, D.: Highly sensitive hot electron bolometer based on disordered graphene. *Sci. Rep.* **3**, 3533 (2013)
43. El Fatimy, A., Myers-Ward, R.L., Boyd, A.K., Daniels, K.M., Gaskill, D.K., Barbara, P.: Epitaxial graphene quantum dots for high-performance terahertz bolometers. *Nat. Nanotechnol.* **11**, 335–338 (2016)
44. Oostinga, J.B., Heersche, H.B., Liu, X., Morpurgo, A.F., Vandersypen, L.M.: Gate-induced insulating state in bilayer graphene devices. *Nat. Mater.* **7**, 151–157 (2008)
45. Xia, F., Farmer, D.B., Lin, Y.M., Avouris, P.: Graphene field-effect transistors with high on/off current ratio and large transport band gap at room temperature. *Nano Lett.* **10**, 715–718 (2010)

46. Vora, H., Kumaravivel, P., Nielsen, B., Du, X.: Bolometric response in graphene based superconducting tunnel junctions. *Appl. Phys. Lett.* **100**, 153507 (2012)
47. Freitag, M., Low, T., Zhu, W., Yan, H., Xia, F., Avouris, P.: Photocurrent in graphene harnessed by tunable intrinsic Plasmons. *Nat. Commun.* **4**, 1951 (2013)
48. Fang, Z., Wang, Y., Liu, Z., Schlather, A., Ajayan, P.M., Koppens, F.H., Nordlander, P., Halas, N.J.: Plasmon-induced doping of graphene. *ACS Nano.* **6**, 10222–10228 (2012)
49. Echtermeyer, T.J., Britnell, L., Jasnós, P.K., Lombardo, A., Gorbachev, R.V., Grigorenko, A.N., Geim, A.K., Ferrari, A.C., Novoselov, K.S.: Strong Plasmonic enhancement of Photovoltage in graphene. *Nat. Commun.* **2**, 458 (2011)
50. Schedin, F., Lidorikis, E., Lombardo, A., Kravets, V.G., Geim, A.K., Grigorenko, A.N., Novoselov, K.S., Ferrari, A.C.: Surface-enhanced Raman spectroscopy of graphene. *ACS Nano.* **4**, 5617–5626 (2010)
51. Mertens, J., Eiden, A.L., Sigle, D.O., Huang, F., Lombardo, A., Sun, Z., Sundaram, R.S., Colli, A., Tserkezis, C., Aizpurua, J., Milana, S., Ferrari, A.C., Baumberg, J.J.: Controlling subnanometer gaps in Plasmonic dimers using graphene. *Nano Lett.* **13**, 5033–5038 (2013)
52. Liu, Y., Cheng, R., Liao, L., Zhou, H., Bai, J., Liu, G., Liu, L., Huang, Y., Duan, X.: Plasmon resonance enhanced multicolour photodetection by graphene. *Nat. Commun.* **2**, 579 (2011)
53. Thongrattanasiri, S., Koppens, F.H., Garcia de Abajo, F.J.: Complete optical absorption in periodically patterned graphene. *Phys. Rev. Lett.* **108**, 047401 (2012)
54. Konstantatos, G., Badioli, M., Gaudreau, L., Osmond, J., Bernechea, M., Garcia de Arquer, F.P., Gatti, F., Koppens, F.H.: Hybrid graphene-quantum dot phototransistors with ultrahigh gain. *Nat. Nanotechnol.* **7**, 363–368 (2012)
55. Rowe, M.A., Gansen, E.J., Greene, M., Hadfield, R.H., Harvey, T.E., Su, M.Y., Nam, S.W., Mirin, R.P., Rosenber, D.: Single-photon detection using a quantum dot optically gated field-effect transistor with high internal quantum efficiency. *Appl. Phys. Lett.* **89**, 253505 (2006)
56. Guo, W., Xu, S., Wu, Z., Wang, N., Loy, M.M., Du, S.: Oxygen-assisted charge transfer between ZnO quantum dots and graphene. *Small.* **9**, 3031–3036 (2013)
57. McDonald, S.A., Konstantatos, G., Zhang, S., Cyr, P.W., Klem, E.J., Levina, L., Sargent, E.H.: Solution-processed Pbs quantum dot infrared photodetectors and photovoltaics. *Nat. Mater.* **4**, 138–142 (2005)
58. Liu, Z., Lau, S.P., Yan, F.: Functionalized graphene and other two-dimensional materials for photovoltaic devices: device design and processing. *Chem. Soc. Rev.* **44**, 5638–5679 (2015)
59. Riazimehr, S., Kataria, S., Bornemann, R., Bolivar, P.H., Ruiz, F.J.G., Engstrom, O., Godoy, A., Lemme, M.C.: High photocurrent in gated graphene-silicon hybrid photodiodes. *ACS Photonics.* **4**, 1506–1514 (2017)
60. Riazimehr, S., Kataria, S., Gonzalez-Medina, J.M., Wagner, S., Shaygan, M., Suckow, S., Ruiz, F.G., Engström, O., Godoy, A., Lemme, M.C.: High responsivity and quantum efficiency of graphene/silicon photodiodes achieved by interdigitating Schottky and gated regions. *ACS Photonics.* **6**(107), 107–115 (2018)
61. Amirmazlaghani, M., Raissi, F., Habibpour, O., Vukusic, J., Stake, J.: Graphene-Si Schottky Ir detector. *IEEE J. Quantum Electron.* **49**(589), 589–594 (2013)
62. Huang, K., Yan, Y., Li, K., Khan, A., Zhang, H., Pi, X., Yu, X., Yang, D.: High and fast response of a graphene-silicon photodetector coupled with 2d fractal platinum nanoparticles. *Adv. Optical Mat.* **6**, 1700793 (2018)
63. Xiang, D., Han, C., Hu, Z., Lei, B., Liu, Y., Wang, L., Hu, W.P., Chen, W.: Surface transfer doping-induced, high-performance graphene/silicon Schottky junction-based, self-powered photodetector. *Small.* **11**, 4829–4836 (2015)
64. Li, X., Zhu, M., Du, M., Lv, Z., Zhang, L., Li, Y., Yang, Y., Yang, T., Li, X., Wang, K., Zhu, H., Fang, Y.: High detectivity graphene-silicon heterojunction photodetector. *Small.* **12**, 595–601 (2016)
65. Kim, J., Joo, S.S., Lee, K.W., Kim, J.H., Shin, D.H., Kim, S., Choi, S.H.: Near-ultraviolet-sensitive graphene/porous silicon photodetectors. *ACS Appl. Mater. Interfaces.* **6**, 20880–20886 (2014)
66. Luo, L.B., Zeng, L.H., Xie, C., Yu, Y.Q., Liang, F.X., Wu, C.Y., Wang, L., Hu, J.G.: Light trapping and surface Plasmon enhanced high-performance Nir photodetector. *Sci. Rep.* **4**, 3914 (2014)
67. Babichev, A.V., Zhang, H., Lavenus, P., Julien, F.H., Egorov, A.Y., Lin, Y.T., Tu, L.W., Tchernycheva, M.: Gan nanowire ultraviolet photodetector with a graphene transparent contact. *Appl. Phys. Lett.* **103**, 201103 (2013)
68. Luo, L.-B., Chen, J.-J., Wang, M.-Z., Hu, H., Wu, C.-Y., Li, Q., Wang, L., Huang, J.-A., Liang, F.-X.: Near-infrared light photovoltaic detector based on Gaas Nanocone Array/monolayer graphene Schottky junction. *Adv. Funct. Mater.* **24**(2794), 2794–2800 (2014)
69. Lee, C.-J., Kang, S.-B., Cha, H.-G., Won, C.-H., Hong, S.-K., Cho, B.-J., Park, H., Lee, J.-H., Hahm, S.-H.: Gan metal-semiconductor-metal Uv sensor with multi-layer graphene as Schottky electrodes. *Jpn. J. Appl. Phys.* **54**, 06ff08 (2015)
70. Luo, L.-B., Hu, H., Wang, X.-H., Lu, R., Zou, Y.-F., Yu, Y.-Q., Liang, F.-X.: A graphene/Gaas near-infrared photodetector enabled by interfacial passivation with fast response and high sensitivity. *J. Mater. Chem. C.* **3**(4723), 4723–4728 (2015)
71. Baeg, K.J., Binda, M., Natali, D., Caironi, M., Noh, Y.Y.: Organic light detectors: photodiodes and phototransistors. *Adv. Mater.* **25**, 4267–4295 (2013)
72. Jang, S., Hwang, E., Lee, Y., Lee, S., Cho, J.H.: Multifunctional graphene optoelectronic devices capable of detecting and storing photonic signals. *Nano Lett.* **15**, 2542–2547 (2015)
73. Liu, X., Luo, X., Nan, H., Guo, H., Wang, P., Zhang, L., Zhou, M., Yang, Z., Shi, Y., Hu, W., Ni, Z., Qiu, T., Yu, Z., Xu, J.B., Wang, X.: Epitaxial ultrathin organic crystals on graphene for high-efficiency phototransistors. *Adv. Mater.* **28**, 5200–5205 (2016)
74. Lee, Y., Kwon, J., Hwang, E., Ra, C.H., Yoo, W.J., Ahn, J.H., Park, J.H., Cho, J.H.: High-performance perovskite-graphene hybrid photodetector. *Adv. Mater.* **27**, 41–46 (2015)
75. Dang, V.Q., Han, G.-S., Trung, T.Q., Duy, L.T., Jin, Y.-U., Hwang, B.-U., Jung, H.-S., Lee, N.-E.: Methylammonium lead iodide perovskite-graphene hybrid channels in flexible broadband phototransistors. *Carbon.* **105**(353), 353–361 (2016)
76. Chang, P.H., Liu, S.Y., Lan, Y.B., Tsai, Y.C., You, X.Q., Li, C.S., Huang, K.Y., Chou, A.S., Cheng, T.C., Wang, J.K., Wu, C.I.: Ultrahigh responsivity and detectivity graphene-perovskite hybrid phototransistors by sequential vapor deposition. *Sci. Rep.* **7**, 46281 (2017)
77. Xie, C., Yan, F.: Perovskite/poly(3-Hexylthiophene)/graphene multiheterojunction phototransistors with ultrahigh gain in broadband wavelength region. *ACS Appl. Mater. Interfaces.* **9**, 1569–1576 (2017)
78. Liu, H., Du, Y., Deng, Y., Ye, P.D.: Semiconducting black phosphorus: synthesis, transport properties and electronic applications. *Chem. Soc. Rev.* **44**, 2732–2743 (2015)
79. Xia, F., Wang, H., Jia, Y.: Rediscovering black phosphorus as an anisotropic layered material for optoelectronics and electronics. *Nat. Commun.* **5**, 4458 (2014)
80. Castellanos-Gomez, A., Barkelid, M., Goossens, A.M., Calado, V.E., van der Zant, H.S., Steele, G.A.: Laser-thinning of Mos(2): on demand generation of a single-layer semiconductor. *Nano Lett.* **12**, 3187–3192 (2012)

81. Mattheiss, L.F.: Band structures of Transition-Metal-Dichalcogenide layer compounds. *Phys. Rev. B.* **8**(3719), 3719–3740 (1973)
82. Song, L., Ci, L., Lu, H., Sorokin, P.B., Jin, C., Ni, J., Kvashnin, A.G., Kvashnin, D.G., Lou, J., Yakobson, B.I., Ajayan, P.M.: Large scale growth and characterization of atomic hexagonal boron nitride layers. *Nano Lett.* **10**, 3209–3215 (2010)
83. Massicotte, M., Schmidt, P., Violla, F., Schadler, K.G., Reserbat-Plantey, A., Watanabe, K., Taniguchi, T., Tielrooij, K.J., Koppens, F.H.: Picosecond Photoresponse in Van Der Waals Heterostructures. *Nat. Nanotechnol.* **11**, 42–46 (2016)
84. Long, M., Liu, E., Wang, P., Gao, A., Xia, H., Luo, W., Wang, B., Zeng, J., Fu, Y., Xu, K., Zhou, W., Lv, Y., Yao, S., Lu, M., Chen, Y., Ni, Z., You, Y., Zhang, X., Qin, S., Shi, Y., Hu, W., Xing, D., Miao, F.: Broadband photovoltaic detectors based on an atomically thin Heterostructure. *Nano Lett.* **16**, 2254–2259 (2016)
85. Roy, K., Padmanabhan, M., Goswami, S., Sai, T.P., Ramalingam, G., Raghavan, S., Ghosh, A.: Graphene-Mos2 hybrid structures for multifunctional Photoresponsive memory devices. *Nat. Nanotechnol.* **8**, 826–830 (2013)
86. Tan, H., Fan, Y., Zhou, Y., Chen, Q., Xu, W., Warner, J.H.: Ultrathin 2d photodetectors utilizing chemical vapor deposition grown Ws2 with graphene electrodes. *ACS Nano.* **10**, 7866–7873 (2016)
87. Liu, Y., Shivananju, B.N., Wang, Y., Zhang, Y., Yu, W., Xiao, S., Sun, T., Ma, W., Mu, H., Lin, S., Zhang, H., Lu, Y., Qiu, C.W., Li, S., Bao, Q.: Highly efficient and air-stable infrared photodetector based on 2d layered graphene-black phosphorus Heterostructure. *ACS Appl. Mater. Interfaces.* **9**, 36137–36145 (2017)
88. Mudd, G.W., Svatek, S.A., Hague, L., Makarovskiy, O., Kudrynskiy, Z.R., Mellor, C.J., Beton, P.H., Eaves, L., Novoselov, K.S., Kovalyuk, Z.D., Vdovin, E.E., Marsden, A.J., Wilson, N.R., Patane, A.: High broad-band Photoresponsivity of mechanically formed Inse-graphene Van Der Waals Heterostructures. *Adv. Mater.* **27**, 3760–3766 (2015)
89. Furchi, M., Urich, A., Pospischil, A., Lilley, G., Unterrainer, K., Detz, H., Klang, P., Andrews, A.M., Schrenk, W., Strasser, G., Mueller, T.: Microcavity-integrated graphene photodetector. *Nano Lett.* **12**, 2773–2777 (2012)
90. Efetov, D.K., Shiue, R.J., Gao, Y., Skinner, B., Walsh, E.D., Choi, H., Zheng, J., Tan, C., Grosso, G., Peng, C., Hone, J., Fong, K.C., Englund, D.: Fast thermal relaxation in cavity-coupled graphene bolometers with a Johnson noise read-out. *Nat. Nanotechnol.* **13**, 797–801 (2018)
91. Engel, M., Steiner, M., Lombardo, A., Ferrari, A.C., Lohneysen, H.V., Avouris, P., Krupke, R.: Light-matter interaction in a microcavity-controlled graphene transistor. *Nat. Commun.* **3**, 906 (2012)
92. Wang, X., Cheng, Z., Xu, K., Tsang, H.K., Xu, J.-B.: High-responsivity graphene/silicon-Heterostructure waveguide photodetectors. *Nat. Photonics.* **7**(888), 888–891 (2013)
93. Goykhman, I., Sassi, U., Desiatov, B., Mazurski, N., Milana, S., de Fazio, D., Eiden, A., Khurgin, J., Shappir, J., Levy, U., Ferrari, A.C.: On-Chip integrated, silicon-graphene Plasmonic Schottky photodetector with high responsivity and avalanche Photogain. *Nano Lett.* **16**, 3005–3013 (2016)
94. Gao, Y., Tao, L., Tsang, H.K., Shu, C.: Graphene-on-silicon nitride waveguide photodetector with interdigital contacts. *Appl. Phys. Lett.* **112** (2018)
95. Naiini, M.M., Vaziri, S., Smith, A.D., Lemme, M.C., Ostling, M.: Embedded graphene photodetectors for silicon photonics. *Proc. 72nd Device Res. Conf.*, 43–44 (2014). <https://doi.org/10.1109/drc.2014.6872291>
96. Li, M., Pernice, W.H., Xiong, C., Baehr-Jones, T., Hochberg, M., Tang, H.X.: Harnessing optical forces in integrated photonic circuits. *Nature.* **456**, 480–484 (2008)
97. Li, H., Anugrah, Y., Koester, S.J., Li, M.: Optical absorption in graphene integrated on silicon waveguides. *Appl. Phys. Lett.* **101**, 111110 (2012)
98. Pospischil, A., Humer, M., Furchi, M.M., Bachmann, D., Guider, R., Fromherz, T., Mueller, T.: Cmos-compatible graphene photodetector covering all optical communication bands. *Nat. Photonics.* **7**(892), 892–896 (2013)
99. Gan, X., Shiue, R.-J., Gao, Y., Meric, I., Heinz, T.F., Shepard, K., Hone, J., Assefa, S., Englund, D.: Chip-integrated ultrafast graphene photodetector with high responsivity. *Nat. Photonics.* **7**(883), 883–887 (2013)
100. Ma, Q., Lui, C.H., Song, J.C.W., Lin, Y., Kong, J.F., Cao, Y., Dinh, T.H., Nair, N.L., Fang, W., Watanabe, K., Taniguchi, T., Xu, S.-Y., Kong, J., Palacios, T., Gedik, N., Gabor, N.M., Jarillo-Herrero, P.: Giant intrinsic Photoresponse in pristine graphene. *Nat. Nanotechnol.* **14**, 145–150 (2019)
101. Yin, J., Peng, H.: Asymmetry allows photocurrent in intrinsic graphene. *Nat. Nanotechnol.* **14**, 105–106 (2019)
102. Lee, W., Liu, Y., Lee, Y., Sharma, B.K., Shinde, S.M., Kim, S.D., Nan, K., Yan, Z., Han, M., Huang, Y., Zhang, Y., Ahn, J.H., Rogers, J.A.: Two-dimensional materials in functional three-dimensional architectures with applications in Photodetection and imaging. *Nat. Commun.* **9**, 1417 (2018)
103. De Fazio, D., Goykhman, I., Yoon, D., Bruna, M., Eiden, A., Milana, S., Sassi, U., Barbone, M., Dumcenco, D., Marinov, K., Kis, A., Ferrari, A.C.: High responsivity, large-area graphene/Mos2 flexible photodetectors. *ACS Nano.* **10**, 8252–8262 (2016)
104. Li, J., Naiini, M.M., Vaziri, S., Lemme, M.C., Östling, M.: Inkjet printing of Mos₂. *Adv. Funct. Mater.* **24**, 6524–6531 (2014)
105. Smith, A.D., Niklaus, F., Pausa, A., Vaziri, S., Fischer, A.C., Sterner, M., Forsberg, F., Delin, A., Esseni, D., Palestri, P., Ostling, M., Lemme, M.C.: Electromechanical Piezoresistive sensing in suspended graphene membranes. *Nano Lett.* **13**, 3237–3242 (2013)
106. Lee, J., Lee, C.-J., Kang, J., Park, H., Kim, J., Choi, M., Park, H.: Multifunctional graphene sensor for detection of environment signals using a decoupling technique. *Solid State Electron.* **151**, 40–46 (2019)



Jiantong Li received his PhD from KTH Royal Institute of Technology, Sweden in 2010. Afterwards, he continued his research at KTH on printed electronics with focus on inkjet printing and 3D printing of graphene and 2D materials for electronics, energy storage, and energy harvesting applications.



Mikael Östling received his PhD from Uppsala University, Sweden. He is a professor and deputy president at KTH Royal Institute of Technology, and an IEEE Life Fellow. He was a Fulbright Scholar at Stanford University, and visiting professor at University of Florida in the US. His research is focused on integrated devices and circuits, focused on emerging materials such as silicon/germanium 3D integration, silicon carbide and 2D materials.